



Analysis of forward scattering of an acoustical zeroth-order Bessel beam from rigid complicated (aspherical) structures



Wei Li^a, Yingbin Chai^a, Zhixiong Gong^{a,b,*}, Philip L. Marston^b

^a School of Naval Architecture and Ocean Engineering, Huazhong University of Science and Technology, Wuhan 430074, PR China

^b Department of Physics and Astronomy, Washington State University, Pullman 99164-2814, WA, USA

ARTICLE INFO

Article history:

Received 24 April 2017

Revised 2 June 2017

Accepted 4 June 2017

Available online 15 June 2017

Keywords:

Forward scattering

Bessel beam

T-matrix method

Ray diagram

Optical theorem

ABSTRACT

The forward scattering from rigid spheroids and endcapped cylinders with finite length (even with a large aspect ratio) immersed in a non-viscous fluid under the illumination of an idealized zeroth-order acoustical Bessel beam (ABB) with arbitrary angles of incidence is calculated and analyzed in the implementation of the T-matrix method (TTM). Based on the present method, the incident coefficients of expansion for the incident ABB are derived and simplifying methods are proposed for the numerical accuracy and computational efficiency according to the geometrical symmetries. A home-made MATLAB software package is constructed accordingly, and then verified and validated for the ABB scattering from rigid aspherical obstacles. Several numerical examples are computed for the forward scattering from both rigid spheroids and finite cylinder, with particular emphasis on the aspect ratios, the half-cone angles of ABBs, the incident angles and the dimensionless frequencies. The rectangular patterns of target strength in the (β, θ_s) domain (where β is the half-cone angle of the ABB and θ_s is the scattered polar angle) and local/total forward scattering versus dimensionless frequency are exhibited, which could provide new insights into the physical mechanisms of Bessel beam scattering by rigid spheroids and finite cylinders. The ray diagrams in geometrical models for the scattering in the forward half-space and the optical cross-section theorem help to interpret the scattering mechanisms of ABBs. This research work may provide an alternative for the partial wave series solution under certain circumstances interacting with ABBs for complicated obstacles and benefit some related works in optics and electromagnetics.

© 2017 Elsevier Ltd. All rights reserved.

1. Introduction

During the past decades, study on acoustic scattering has attained a great development and attracted increasing attention from investigators all over the world. As reported in the literature, there is a wide range of applications for acoustic scattering in practical and potential engineering fields, such as non-destructive testing technology, ultrasonic medical diagnostic imaging technology, sound navigation and ranging (SONAR), sound detection and ranging (SODAR), acoustic Doppler current profiler, acoustic tweezers/torques/levitation devices, and so forth. Specifically, the monostatic and bistatic sonars are designed and manufactured based in part on acoustic scattering theories. The main difference between the monostatic and bistatic sonar devices is the spatial location distribution of acoustic source and receiver, namely, the acoustic source and receiver of the bistatic sonar are spatially separated while those of the monostatic are not. Therefore, it is obvi-

ous to note that the monostatic sonar benefits a lot from research work on backscattering, in contrast for the bistatic sonar, one of its special case (i.e. forward scattering) is widely used in engineering practices since it can provide a large acoustic gain in the forward direction around the target. As claimed in Refs. [1–3], scattering strength in the forward direction is generally stronger than that in the backward scattering. Furthermore, the forward scattering of target is less sensitive to the incidence angle of sound than backscattering which could be applied to calculate scattering from moving targets stably and accurately. Based on the above statements, it is therefore significant and necessary to make further investigations on the forward scattering of a variety of aspects, which may in turn improve the forward scattering theories and benefit several potential applications and engineering practices.

However, most of the published work on the forward scattering in the literature concentrated on the ordinary plane wave incidence case [1–8]. When it comes to acoustical Bessel beams (ABBs), the relevant research on forward scattering is rarely found and the published works in numerical computation were mainly focused on spherical shapes [9,10]. As extensively studied both in optical

* Corresponding author.

E-mail address: hustgzx@hust.edu.cn (Z. Gong).

[11–15] and acoustical fields [16–22], Bessel beams are demonstrated to be one kind of undistorted waves, having shown its own advantages over the plane waves and Gaussian beams for its novel characteristics including the non-diffraction property [23–26] and self-construction ability [27–29]. In general, ABBs are roughly classified into two kinds: the zeroth-order and high orders Bessel beams, with their amplitude profiles proportional to the zeroth-order Bessel function J_0 and higher order Bessel function J_m (m is an integer with $m \geq 1$), respectively. Due to the properties of Bessel functions, it is thus reasonable to find that the zeroth-order ABB has a maximum in amplitude at its center of cross-section profile with concentric rings of decreasing radial amplitude and axisymmetric azimuthal phase, while the higher orders ABBs possess an axial null in amplitude and has an azimuthal phase gradient [17]. It may be helpful to the readers that the form function of the scattering of higher orders ABBs could be deduced as a special case of those of the nondiffracting Lommel beams [30]. Besides, it should be noted that the fractional Bessel beams are not proper solutions of the scalar Helmholtz equation because of the phase discontinuity when the azimuthal angle is $\phi=0$ [31]. Intuitively, the acoustic radiation induced by progressive plane wave scattering tends to push the scatterers away from sources in the propagation direction of the beam, which is here termed as positive radiation force (relative to negative radiation force). Due to the aforementioned characteristics, however, this is not always the case for ABBs. Because of the peculiar features different from those of ordinary plane waves, negative acoustic radiation force [16,32] and even acoustic radiation torque [19,33] could be realized in the context of a single ABB under certain circumstances, which may provide impetus to design acoustic tweezers and torque devices in area of acoustic manipulation and control (pulling, pushing, rotating or levitating particles).

In the recent past decade, the problems of ABBs have been studied by means of analytical, numerical and experimental approaches. However, prior studies using analytical (partial wave series solution) [9,16] and experimental methods [21,22] apparently had their emphasis on the spherical obstacles. For the partial wave series method (PWSM), several principles and novel phenomena of backscattering and bistatic scattering for spherical shapes have been reported [9,16–19]. From the computational standpoint, however, it seems that the PWSM in spherical coordinate frame may fail for the large-aspect-ratio aspherical shapes, such as spheroid and finite cylinder with endcaps. This is due to the fact that the spherical harmonics are employed as the basis functions of expansion and the system of linear equations may become unsolvable because of an ill-condition during matrix inversion procedures [34,35]. When it comes to experimental investigations, the set-ups for producing Bessel beams and receiving scattering signals are usually very expensive and moreover, the generating Bessel beams are not idealized because of the finite power of the sources. In addition, the experiment setup still suffers some technique problems, overheating of transducers for instance [20–22]. Based on the above descriptions, it is therefore reasonable and necessary to introduce the *T*-matrix method (TMM) into the computational area for ABBs since the TMM (a semi-analytical and semi-numerical approach) is a versatile tool to deal with scattering in acoustic [36–42], electromagnetic [43–45] and elastic [46,47] fields. In addition, the TMM has been extended to calculate the acoustic scattering under the illumination of Bessel beams interacting with elastic spherical shapes [48] and spheroids [49].

Nevertheless, to the best of the authors' knowledge, systematic research on the forward scattering of ABBs is somewhat limited, especially for aspherical targets. As is known to all, the versatile TMM was proved to show good convergence and high precision especially for axisymmetric shapes, including spherical and aspherical, rigid and non-rigid targets. In the present article, the TTM will

be further implemented to explore novel and maybe useful phenomena of ABBs in the forward scattering for rigid complicated targets. On the one hand, the present investigation could be expected to enrich the analysis of scattering of ABBs from not only spherical but also aspherical shapes. On the other hand, it may also provide an alternative for the experimental methods when dealing with forward scattering since the forward scattering signals are easily overwhelmed by either the strong direct signals by source or the strong interference between them. It could be therefore anticipated that the TMM will provide a competitive tool to gain insight into the novel scattering properties and also help to interpret the scattering mechanisms of ABBs in the forward half-space.

The frame of this article is outlined as follows. In Section 2, theoretical formulations of the *T*-matrix method for the acoustic scattering by rigid obstacles with arbitrary shapes immersed in fluid are presented briefly, including the derivation of the expansion coefficients of the incident ABBs (Section 2.1), a brief frame of TTM for rigid obstacle (Section 2.2), several numerical methods for the *Q* matrix (Section 2.3) and understandings of form function and target strength (Section 2.4). Subsequently in Section 3.1, convergence study and stability of *Q* matrix are discussed. Section 3.2–3.5 gives several numerical experiments with particular emphasis on scattering in the forward half-space. Finally, some useful concluding remarks are summarized in Section 4.

2. Theoretical formulation

In the formulation of standard *T*-matrix method (TMM), all field quantities (including the incident fields, scattered fields, Green's function and unknown surface fields) are expanded in terms of a set of spherical functions in order to obtain the expected transition matrix (*T* matrix). Specifically, the transition matrix gives a linear relationship between the known coefficients of expansion of the incident wave to the unknown expansion coefficients of the scattered field. It is well known that the incident coefficients of expansion are easily obtained when given a specific scalar basis function for plane wave case. Once the transition matrix is constructed for an object of interest, the scattered fields could be calculated immediately. Likewise, if the acoustic Bessel beams (ABBs), which may be regarded as a superposition of plane waves [9], can be expanded based on an appropriate scalar basis function, the TTM is therefore anticipated to perform very well to solve scattering problems interacted with Bessel beams. So in the following, we will first derive the expansion coefficients of the incident Bessel beam, and then give a brief formula system of TTM for rigid object with arbitrary shapes.

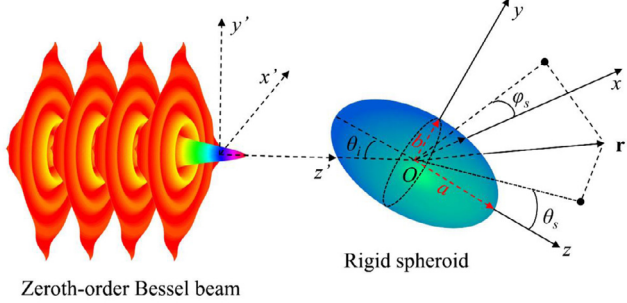
2.1. Expansion coefficients of the incident Bessel beam

Considering an idealized monochromatic zeroth-order Bessel beam (See Fig. 1), which is actually an axisymmetric solution of the Helmholtz equation, the expression of its complex velocity potential could be given [50]

$$\phi_B^i(z, \rho) = \phi_0 \exp(i\kappa z) J_0(\mu\rho) \quad (1)$$

where ϕ_0 is the beam amplitude and i is the unit imaginary number, z and $\rho = \sqrt{x^2 + y^2}$ specify the axial and radial coordinates, $\kappa = k\cos\beta$ and $\mu = k\sin\beta$, satisfying the relation $\kappa^2 + \mu^2 = k^2$, represent the axial and radial wavenumbers, and J_0 is a zeroth-order cylindrical Bessel function of the first kind. Here in Eq. (1), the complex time factor of the form $\exp(-i\omega t)$ has been separated from the spatial dependence of the complex functions. It should be further noted that all field quantities will also have the same harmonic time dependence due to the incident wave, and hence the time dependence will be factored out throughout for convenience.

(a)



Zeroth-order Bessel beam

(b)

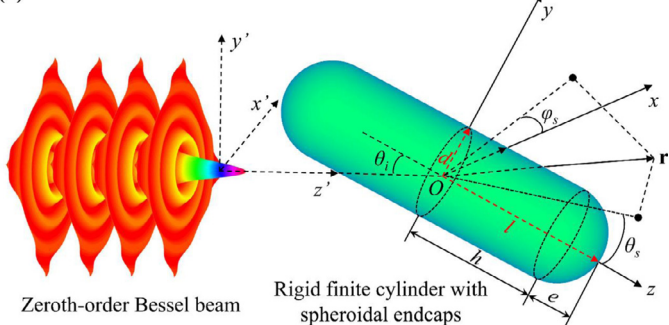


Fig. 1. The schematic of a rigid (a) spheroid and (b) finite cylinder with hemispherical endcaps placed in a monochromatic zeroth-order Bessel beam with arbitrary angles of incidence in a spherical coordinates system. θ_i denotes the axial angle of the incident Bessel beam while θ_s and φ_s specify the axial and azimuthal angles of observation.

The incident zeroth-order Bessel beam $\phi_B^i(z, \rho)$ could be expanded in spherical coordinates (r, θ, ϕ) as given by Eq. (B2) in Appendix B [9] in the following expression:

$$\phi_B^i(r, \theta) = \phi_0 \sum_{n=0}^{\infty} i^n \times (2n+1) j_n(kr) P_n(\cos \theta) P_n(\cos \beta) \quad (2)$$

where β denotes half-cone angle of the Bessel beam and θ is the polar angle of the incident wave with respect to a given spherical basis function. To extend the application of TTM for ABB scattering problems, there is a need to expand the incident Bessel beams on the basis of the given scalar basis function. To this end, the widely-used scalar basis function in spherical coordinate system is therefore introduced as

$$\phi_{nm\sigma}(\mathbf{r}) = \xi_{nm} h_n(kr) P_n^m(\cos \theta_b) \begin{cases} \cos(m\varphi_b), & \sigma = e \\ \sin(m\varphi_b), & \sigma = o \end{cases} \quad (3)$$

where,

$$\xi_{nm} = \left(\varepsilon_m \frac{(2n+1)(n-m)!}{4\pi(n+m)!} \right)^{1/2} \quad (4)$$

and $h_n(kr)$ is the spherical Hankel function of the first kind, $P_n^m(\cos \theta_b)$ is the associated Legendre function and $\varepsilon_m = 2 - \delta_{m0}$ denotes the Neumann factor. $\sigma = e, o$ (even, odd) specifies the azimuthal parity, $m = 0, 1, \dots, n$ specifies the rank, and $n = 0, 1, \dots, \infty$ specifies the order of the spherical wave functions.

Noted that the incident fields are actually finite at the origin, the spherical Hankel function of the first kind (which is singular at the origin) in Eq. (3) should be replaced by the spherical Bessel function of the first kind $j_n(kr)$ which is regular at the origin. Therefore, we can use the revised basis function to expand the incident field, with the expression denoted by $\text{Re}\phi_{nm\sigma}$:

$$\text{Re}\phi_{nm\sigma}(\mathbf{r}) = \xi_{nm} j_n(kr) P_n^m(\cos \theta_b) \begin{cases} \cos(m\varphi_b), & \sigma = e \\ \sin(m\varphi_b), & \sigma = o \end{cases} \quad (5)$$

In order to expand the incident zeroth-order Bessel beam (Eq. (2)) based on the foregoing spherical basis functions (Eq. (5)), the addition theorem for the Legendre polynomials is utilized accordingly with the desired expansion as follows [51]

$$P_n(\cos \theta) = \sum_{m=0}^n \varepsilon_m \frac{(n-m)!}{(n+m)!} \times P_n^m(\cos \theta_i) P_n^m(\cos \theta_b) \cos m(\varphi_i - \varphi_b) \quad (6)$$

where (θ_i, φ_i) and (θ_b, φ_b) stand for the spherical coordinates of incident and basis wave functions, respectively.

Substituting Eqs. (5) and (6) into Eq. (2), the complex velocity potential of the zeroth-order Bessel beam could be expressed according to a product form as

$$\phi_B^i(r, \theta) = a_{nm\sigma} \times \text{Re}\phi_{nm\sigma}(\mathbf{r}) \quad (7)$$

where $a_{nm\sigma}$ stands for the expansion coefficients of the incident unbounded zeroth-order Bessel beam given in detail by

$$a_{nm\sigma} = 4\pi \xi_{nm} i^n \times P_n^m(\cos \theta_i) P_n(\cos \beta) \begin{cases} \cos(m\varphi_i), & \sigma = e \\ \sin(m\varphi_i), & \sigma = o \end{cases} \quad (8)$$

It should be noted that the expression of the expansion coefficients $a_{nm\sigma}$ depends on the half-cone angle β , as well as the incident axial angles θ_i and azimuthal angles φ_i . For Bessel beams, the half-cone angle β is a characteristic parameter which is in fact the angle describing the plane wave vector component with respect to the beam axis. In particular, when the half-cone angle is selected as $\beta = 0^\circ$, the zeroth-order Bessel beam will actually degrade into an ordinary plane wave. It is necessary to note that the incident axial angle θ_i could vary from 0° to 360° (i.e. arbitrary angles of incidence). In addition, there is also potential for the TTM to calculate the scattering from high orders Bessel beams in case that the expansion coefficients of the high order ABBs could be derived based on an appropriate basis function, however, that case is outside the scope of the present investigation.

2.2. T-matrix method for arbitrary rigid shape in an ideal fluid

Section 2.1 makes it clear that the TMM may be a possible tool for scattering in Bessel beams because of the fact that the incident zeroth-order Bessel beam could be expanded in a product form of the expansion coefficients and spherical basis function. In the following, the transition matrix will be briefly derived according to the most relevant formula to obtain the desired scattered fields (expansion coefficients of the scattering fields) illuminated by ABBs. Note that there are three parts in need to obtain the transition matrix: the integral representations for the velocity potentials (null-field equation), the expansions of surface fields and the corresponding boundary conditions.

Consider a rigid obstacle with arbitrary shape immersed in an infinite, homogeneous and nonviscous fluid. The rigid object with surface S is placed in an acoustic monochromatic zeroth-order Bessel beam at an arbitrary angle of incidence, with the surrounding ideal fluid having a sound velocity c and a density ρ . As mentioned above, the time factor $\exp(-i\omega t)$ is suppressed throughout since all fields have the same harmonic time-dependence. At the beginning, the relevant acoustical velocity potentials in the Bessel beam are given by the following expression

$$\phi_B(\mathbf{r}) = \phi_B^i(\mathbf{r}) + \phi_B^s(\mathbf{r}) \quad (9)$$

where $\phi_B(\mathbf{r})$ denotes the total velocity potential in fluid, which is in the form of sum of the incident ($\phi_B^i(\mathbf{r})$) and the scattered ($\phi_B^s(\mathbf{r})$) velocity potentials. Note that all the above velocity poten-

tials satisfy the Helmholtz equation which can be written as

$$(\nabla^2 + k^2) \begin{pmatrix} \phi_B(\mathbf{r}) \\ \phi_B^i(\mathbf{r}) \\ \phi_B^s(\mathbf{r}) \end{pmatrix} = 0 \quad (10)$$

where $k=\omega/c$ is the wave number in the surrounding fluid and ω specifies the angular frequency. Then, the integral representation (also called the null-field equation), which are originally presented in Waterman's paper on the T-matrix formulation of acoustic wave scattering [36], are given by

$$\phi_B^i(\mathbf{r}) + \int_S [\phi_+ \bar{\mathbf{n}} \cdot \nabla g(\mathbf{r}, \mathbf{r}') - (\bar{\mathbf{n}} \cdot \nabla_+ \phi) g(\mathbf{r}, \mathbf{r}')] dS \\ = \begin{cases} \phi_B(\mathbf{r}) & \mathbf{r} \text{ outside } S \\ 0 & \mathbf{r} \text{ inside } S \end{cases} \quad (11)$$

where

$$g(\mathbf{r}, \mathbf{r}') = \exp(ik|\mathbf{r} - \mathbf{r}'|)/(k|\mathbf{r} - \mathbf{r}'|) \quad (12)$$

is the free space Green's function of the Helmholtz equation. S represents the surface of considered object and $\bar{\mathbf{n}}$ denotes the continuous turning unit normal taken as outward pointing. The quantities ϕ_+ and $\bar{\mathbf{n}} \cdot \nabla_+ \phi$ stand for the velocity potential and normal component of the velocity on the outside of surface S , respectively.

Next, all quantity fields relevant to the derivation of transition matrix, including the velocity potentials of the incident $\phi_B^i(\mathbf{r})$ and scattered fields $\phi_B^s(\mathbf{r})$ in ABBs, the Green's function $g(\mathbf{r}, \mathbf{r}')$ and the unknown surface fields $\phi_+(\mathbf{r})$, should be expanded in terms of a set of spherical harmonic functions (i.e. appropriate basis set). As a consequence, the velocity potentials of the incident and scattered fields can be expanded as

$$\phi_B^i(\mathbf{r}) = \sum_{n=0}^{\infty} \sum_{m=0}^n \sum_{\sigma} a_{nm\sigma} \operatorname{Re} \phi_{nm\sigma}(\mathbf{r}) \quad (13)$$

$$\phi_B^s(\mathbf{r}) = \sum_{n=0}^{\infty} \sum_{m=0}^n \sum_{\sigma} f_{nm\sigma} \phi_{nm\sigma}(\mathbf{r}) \quad (14)$$

where $a_{nm\sigma}$ are the known coefficients of the incident Bessel beam (given in Eq. (8)) and $f_{nm\sigma}$ are the desired unknown coefficients of the scattered fields, respectively. Note that the infinite summation in Eqs. (13) and (14), which is indeed available in theory, must be truncated at an appropriate limit n_{\max} from the standpoint of numerical computation. This limit should be judiciously chosen so that high precision and adequate convergence of the truncated series are warranted. The numerical details will be exhibited and discussed by a convergence study in the numerical examples.

In addition to the expansions of the incident and scattered fields, the Green's function $g(\mathbf{r}, \mathbf{r}')$ and the unknown surface field ϕ_+ are also expanded in the following forms, respectively

$$g(\mathbf{r}, \mathbf{r}') = ik \sum_n \sum_m \sum_{\sigma} \phi_{nm\sigma}(r_>) \operatorname{Re} \phi_{nm\sigma}(r_<) \quad (15)$$

$$\phi_+(\mathbf{r}) = \sum_n \sum_m \sum_{\sigma} \alpha_{nm\sigma} \phi_{nm\sigma}(\mathbf{r}) \quad (16)$$

where $r_> = \max(r, r')$ and $r_< = \min(r, r')$, with r' being the distance of considered field points to the origin and r the distance of points on the surface S to the origin. Here, $\alpha_{nm\sigma}$ denotes the expansion coefficients of surface fields, which is finally eliminated in the procedure to obtain the transition matrix (connecting $f_{nm\sigma}$ and $a_{nm\sigma}$).

For the perfectly rigid obstacle with an arbitrary shape under consideration, the Neumann boundary condition is imposed on the surface of the object at $\mathbf{r}=S(\theta)$, such that

$$\bar{\mathbf{n}} \cdot \nabla_+ \phi(\mathbf{r}) \Big|_{\mathbf{r}=S(\theta)} = 0 \quad (17)$$

Note that the TTM could be also implemented for different boundary conditions, such as the Dirichlet (sound soft) and impedance boundary conditions. In each case, the integral representation in Eq. (11) may be simplified by choosing different expressions for the unknown surface fields ϕ_+ or $\bar{\mathbf{n}} \cdot \nabla_+ \phi$. However, only the Neumann boundary condition is in the scope of the present work. Finally, all the formula which are needed to acquire the desired transition matrix are available, including the integral representations Eq. (11), the expansions of all fields (Eqs. (13)–(16)) and the corresponding boundary condition (Eq. (17)). Consequently, the transition matrix can be derived immediately and given by Waterman in an obvious matrix notation as

$$f = Ta \quad (18)$$

where T is the transition matrix (T matrix) of a considered rigid obstacle given by

$$T = -(\operatorname{Re} Q) Q^{-1} \quad (19)$$

Specially, the elements of Q matrix are written as

$$Q_{nm,n'm'}^{\sigma\sigma'} = \int_S \operatorname{Re} \phi_{n'm'\sigma'} \bar{\mathbf{n}} \cdot \nabla \phi_{nm\sigma} dS \quad (20)$$

In particular, the properties of transition matrix relate closely on those of the Q matrix in a straightforward way. Moreover, the transition matrix depends solely on the wavelength, the geometrical shape and material composition (with respect to the surrounding medium) of the scatterer, and is otherwise independent of the incident source. Theoretically, the transition method could be employed for obstacles with arbitrary shapes as long as the explicit shape functions are given in a computational way. In practice, as demonstrated by several pioneers of this versatile method, the TTM are exceptionally efficient for objects with symmetries, such as rotational and axial symmetries, due to the fact that symmetries would greatly reduce the number and complexity of the matrix elements. In the present investigation, numerical experiments of two typical aspherical shapes (both in the nature and engineering practice), namely the rigid spheroids and spherically endcapped cylinders with finite length, are carried out and discussed using the transition method, and thus providing a powerful numerical tool to study the Bessel beam scattering except for partial-wave series solution.

The schematics of a monochromatic zeroth-order Bessel beam illuminating on a perfectly rigid spheroid and finite cylinder at arbitrary angles of incidence in a spherical coordinates system are depicted in Fig. 1(a) and (b), respectively. In order to obtain the Q matrix, as described by Eq. (20), an integral must be implemented over the surface of the considered obstacle. Hence, the corresponding shape functions of the rigid spheroid and cylinder are expressed with their geometric parameters afterwards. Note that for both the spheroid and finite cylinder, there is an azimuthal symmetry of the geometrical shapes, leading to the surface shape functions $S(\theta)$ only dependent on the polar angle θ . Subsequently, the corresponding explicit representations of shape functions for a rigid spheroid and cylinder are given separately below. First, for the rigid spheroid, the shape function of the surface is given by

$$S(\theta) = (\cos^2 \theta / a^2 + \sin^2 \theta / b^2)^{-1/2} \quad (21)$$

where the parameter a denotes the polar radius (the length between the center and the endpoint of spheroid along its rotation axis of symmetry) and b denotes the equatorial radius. Note that a prolate spheroid is defined when the polar radius is larger than the equatorial radius ($a > b$), as depicted by Fig. 1(a), whereas an oblate spheroid is defined when $a < b$ (not shown here for brevity). Especially, in the case of $a=b$, the spheroid degenerates to a sphere, whose surface shape function $S(\theta)$ no longer depends

on the polar angle θ , the special case will also be discussed in the section of numerical examples.

Second, for the rigid finite cylinder with two hemispherical endcaps as described in Fig. 1(b), the shape function of the surface:

$$S(\theta) = \begin{cases} h \cos \theta + \sqrt{e^2 - h^2 \sin^2 \theta}, & 0 < \theta < \theta_0, \\ h/\cos \theta, & \theta_0 < \theta < \pi - \theta_0, \\ -h \cos \theta + \sqrt{e^2 - h^2 \sin^2 \theta} & \pi - \theta_0 < \theta < \pi, \end{cases} \quad (22)$$

where e stands for the polar radius of the endcap, h specifies the half length of the cylindrical portion, and therefore the half-length of the finite cylinder with endcaps is $l=h+e$ (which will be used in the numerical section). The parameter θ_0 is the angle of the critical point that connects the cylindrical section with the endcap on the surface $S(\theta)$, writing

$$\theta_0 = \cos^{-1}\left(h/\sqrt{h^2 + d^2}\right) \quad (23)$$

Here, d denotes the radius of the finite cylinder. Note that when $e=d$, the endcaps become hemispheres, which will be considered in numerical examples in our present investigation. Moreover, other complex geometrical shapes could be also studied through TMM immediately, such as finite cylinder with spheroidal endcaps ($e \neq d$) [42] and Peanut-shaped (shape function $S(\theta) = (\cos^2 \theta/a^2 + \sin^2 \theta/b^2)^{1/2}$) obstacles [52], once their corresponding surface shape functions are available in an explicit numerical expression.

2.3. Structure of Q matrix and properties of symmetry

To emphasize the advantages of the present matrix method and get a better understanding of the elements in matrices, it is thus necessary to examine and discuss the structure of the Q matrix for obstacles which possess rotational and mirror symmetries in our study. One notes that the indices of the elements in Q matrix are denoted by $(nm\sigma, n'm'\sigma')$, hence, it is noticeably convenient to break the Q matrix into four blocks according to the azimuthal parity such that

$$Q = \begin{bmatrix} Q_{nm,n'm'}^{ee} & Q_{nm,n'm'}^{eo} \\ Q_{nm,n'm'}^{oe} & Q_{nm,n'm'}^{oo} \end{bmatrix} \quad (24)$$

where for each block with an even parity, there is $n=0, 1, \dots, \infty$ and $m=0, 1, \dots, n$, otherwise with an odd parity, $n=0, 1, \dots, \infty$ and $m=1, 2, \dots, n$ should be employed.

It should be noted that the index n could not approach infinity from the point of numerical calculation in practice, and thus, it must be truncated at an appropriate limit n_{\max} which can ensure both the accuracy and efficiency of the transition method at the same time. Generally, a rough rule is to set the truncation limit as $n_{\max}=6+\text{Int}(ka)$ [53], with the $\text{Int}(ka)$ being the integer part of the dimensionless frequency ka . Consider a block with the same parity in Q matrix, Q^{ee} for instance. The specific form of element distribution in Q^{ee} when $n=n'=2$ can be written explicitly in the form of matrix (with its size 6×6)

$$Q^{ee} = \begin{bmatrix} Q_{00,00}^{ee} & Q_{00,10}^{ee} & Q_{00,11}^{ee} & Q_{00,20}^{ee} & Q_{00,21}^{ee} & Q_{00,22}^{ee} \\ Q_{10,00}^{ee} & Q_{10,10}^{ee} & Q_{10,11}^{ee} & Q_{10,20}^{ee} & Q_{10,21}^{ee} & Q_{10,22}^{ee} \\ Q_{11,00}^{ee} & Q_{11,10}^{ee} & Q_{11,11}^{ee} & Q_{11,20}^{ee} & Q_{11,21}^{ee} & Q_{11,22}^{ee} \\ Q_{20,00}^{ee} & Q_{20,10}^{ee} & Q_{20,11}^{ee} & Q_{20,20}^{ee} & Q_{20,21}^{ee} & Q_{20,22}^{ee} \\ Q_{21,00}^{ee} & Q_{21,10}^{ee} & Q_{21,11}^{ee} & Q_{21,20}^{ee} & Q_{21,21}^{ee} & Q_{21,22}^{ee} \\ Q_{22,00}^{ee} & Q_{22,10}^{ee} & Q_{22,11}^{ee} & Q_{22,20}^{ee} & Q_{22,21}^{ee} & Q_{22,22}^{ee} \end{bmatrix} \quad (25)$$

Similarly, the forms of element distribution for the case of different parity, taking Q^{eo} as an example, can be acquired at the

same truncation limit ($n=n'=2, m=0, 1, 2$ and $m'=1, 2$).

$$Q^{eo} = \begin{bmatrix} Q_{00,11}^{eo} & Q_{00,21}^{eo} & Q_{00,22}^{eo} \\ Q_{10,11}^{eo} & Q_{10,21}^{eo} & Q_{10,22}^{eo} \\ Q_{11,11}^{eo} & Q_{11,21}^{eo} & Q_{11,22}^{eo} \\ Q_{20,11}^{eo} & Q_{20,21}^{eo} & Q_{20,22}^{eo} \\ Q_{21,11}^{eo} & Q_{21,21}^{eo} & Q_{21,22}^{eo} \\ Q_{22,11}^{eo} & Q_{22,21}^{eo} & Q_{22,22}^{eo} \end{bmatrix} \quad (26)$$

where the size of Q^{eo} block is 6×3 . Likewise, the sizes of Q^{oe} and Q^{oo} could be also obtained as 3×6 and 3×3 , respectively. Consequently, the total size of the Q matrix (including the above four blocks) is 9×9 when n_{\max} equals to 2, and thus the total size could be summed up as $(n_{\max}+1)^2 \times (n_{\max}+1)^2$ through the mathematical induction. As an example, in the low-frequency region typically for $ka < 1$, the maximum truncation index is $n_{\max}=7$ following the aforementioned general rule and thus the size of the Q matrix is 64×64 . Note that the matrix dimension will become very large for high computational frequencies as the truncation limit increases. Fortunately, several simplifying methods could be implemented due to the properties of symmetry, which will be discussed in detail next.

First, the integral expression of the element in the Q matrix in Eq. (20) could be rewritten in the spherical coordinates systems as

$$Q_{nm,n'm'}^{\sigma\sigma'} = \int_0^\pi \int_0^{2\pi} \text{Re}\phi_{n'm'\sigma'} \vec{n} \cdot \nabla\phi_{nm\sigma} r^2 \sin\theta d\varphi d\theta \quad (27)$$

For an obstacle of a rotational symmetry, the surface shape function $r=S(\theta)$ only depends on the polar angle θ under the circumstance, and is independent of the azimuthal angle φ (i.e. $r_\varphi = \partial r(\theta)/\partial\varphi = 0$). In consequence, one can obtain

$$\vec{n} \cdot \nabla\phi_{nm\sigma} = \frac{\partial\phi}{\partial r} + \frac{r_\theta}{r^2} \frac{\partial\phi}{\partial\theta} \quad (28)$$

where r_θ represents the partial derivative of $r(\theta)$ with respect to the polar angle θ .

Insertion Eqs. (3), (4) and (28) into Eq. (27) facilitates the desired expression:

$$Q_{nm,n'm'}^{\sigma\sigma'} = \int_0^\pi \xi_{n'm'} j_{n'}(kr) P_n^{m'}(\cos\theta) \xi_{nm} \times \left[\frac{\partial h_n(kr)}{\partial r} P_n^m(\cos\theta) - \frac{r_\theta}{r^2} h_n(kr) \frac{\partial P_n^m(\cos\theta)}{\partial\theta} \right] \times r^2 \sin\theta d\theta \int_0^{2\pi} \begin{pmatrix} \cos m'\varphi \\ \sin m'\varphi \end{pmatrix} \begin{pmatrix} \cos m\varphi \\ \sin m\varphi \end{pmatrix} d\varphi \quad (29)$$

It is noteworthy that each element in the Q matrix requires computation of the quadric integral involving mixed products of Bessel and Legendre functions on the surface of obstacle, leading to the complexity and a high computational cost to solve the Q matrix of large dimension. Nevertheless, the geometry symmetries (including mirror and rotation symmetries) of the obstacle will dramatically reduce the computational cost of the Q matrix using several simplifying methods, and meanwhile could help to ensure the computational accuracy.

As observed from Eq. (29), one can draw the following conclusions, such that

$$(i) Q_{nm,n'm'}^{eo} = Q_{nm,n'm'}^{oe} = 0;$$

This is due to the fact that the integrals involving mixed products of sines and cosines are seen to vanish (the orthogonality of trigonometric functions). It could be also inferred by the mirror symmetry of the geometrical shapes.

$$(ii) Q_{nm,n'm'}^{ee} = Q_{nm,n'm'}^{oo} = 0 \text{ when } m \neq m';$$

This is because of orthogonality of trigonometric functions that the product of two sines (or cosines) integrating over one cycle also vanishes.

(iii) $Q_{nm,n'm'}^{ee} = Q_{nm,n'm'}^{oo}$ with the exception of $m=0$ or $m'=0$;

It follows the (ii) with $m=m'$, because $\int_0^{2\pi} \cos m'\varphi \cos m'\varphi d\varphi = \int_0^{2\pi} \sin m'\varphi \sin m'\varphi d\varphi$.

All in all, the symmetries significantly reduce the computational cost for the elements of Q matrix by introducing the above simplifying methods. Specifically, the rotational symmetry help to reduce the quadric integrals into line integrals in θ . Moreover, it should be noted that the mirror symmetry helps to need only to compute the matrix elements with the following indices when $(n+n')$ is even, meanwhile, the integration interval can be reduced to $0^\circ \leq \theta \leq 90^\circ$. Under the present circumstances, only the following elements in the block $Q_{nm,n'm'}^{ee}$ need to be calculated, writing

$$Q_{nm,n'm'}^{ee} = \beta_m \xi_{n'm'} \xi_{nm} \int_0^\pi j_{n'}(kr) P_{n'}^{m'}(\cos \theta) \times \left[\frac{\partial h_n(kr)}{\partial r} P_n^m(\cos \theta) - \frac{r_\theta}{r^2} h_n(kr) \frac{\partial P_n^m(\cos \theta)}{\partial \theta} \right] \times r^2 \sin \theta d\theta \quad (30)$$

where $\beta_m = \pi$ in the case of $m \neq 0$, otherwise $\beta_m = 2\pi$.

2.4. Form function and target strength (TS)

To date, all the relevant formula on the acoustic scattering from rigid complicated obstacles illuminated by a zeroth-order Bessel beam using the TTM have been presented above, including several numerical simplifying methods. In fact, the transition method is a versatile tool to calculate scattering from every direction at the arbitrary angles of incidence. However, in the present investigation, we will put the emphasis on the forward scattering, such as scattering in the forward half-space, the total (scattering angle equals to the incident angle of the beam axis) and local (scattering angle equals to the incident angle of local planar waves) forward scattering.

For the ideal zeroth-order ABB illumination, the scattering fields could be computed immediately once the transition matrix of a given obstacle immersed in fluid and the expansion coefficients of the incident fields according to Eqs. (8), (14) and (18). Generally in engineering practice of acoustics, the far-field scattering is often considered when the target-to-receiver range is usually over ten times than the characteristic length dimension of the obstacle (for a sphere, the characteristic length dimension is its diameter). Hence, the far-field form function f_∞ in the frequency domain is introduced which depicts a dimensionless measure of the complex amplitude of the scattered pressure field. In addition, the form function is actually normalized by the pressure of incident field, the target-to-receiver range and a characteristic length dimension of the obstacle from scattered pressure [54]. Based on the above description, a unified form of expression for the far-field form function is defined through the relationship with the far-field velocity potential $\lim_{r \rightarrow \infty} \phi^s$ for a rigid obstacle (actually could be extended for elastic cases) written as

$$\lim_{r \rightarrow \infty} \phi^s = \phi_0 \frac{r_0}{2r_\infty} f_\infty(kr_0, \theta, \varphi, \beta) \exp(ikr_\infty) \quad (31)$$

where r_0 is the radius of the sphere circumscribed the spheroid or the finite cylinder with endcaps, and r_∞ is the distance from the far-field point to the coordinate origin. Notice that the incident pressure amplitude ϕ_0 is measured at the origin in the absence of the obstacle through experimental observations [55]. As observed from Eq. (31) that for the Bessel beam case, the form function is

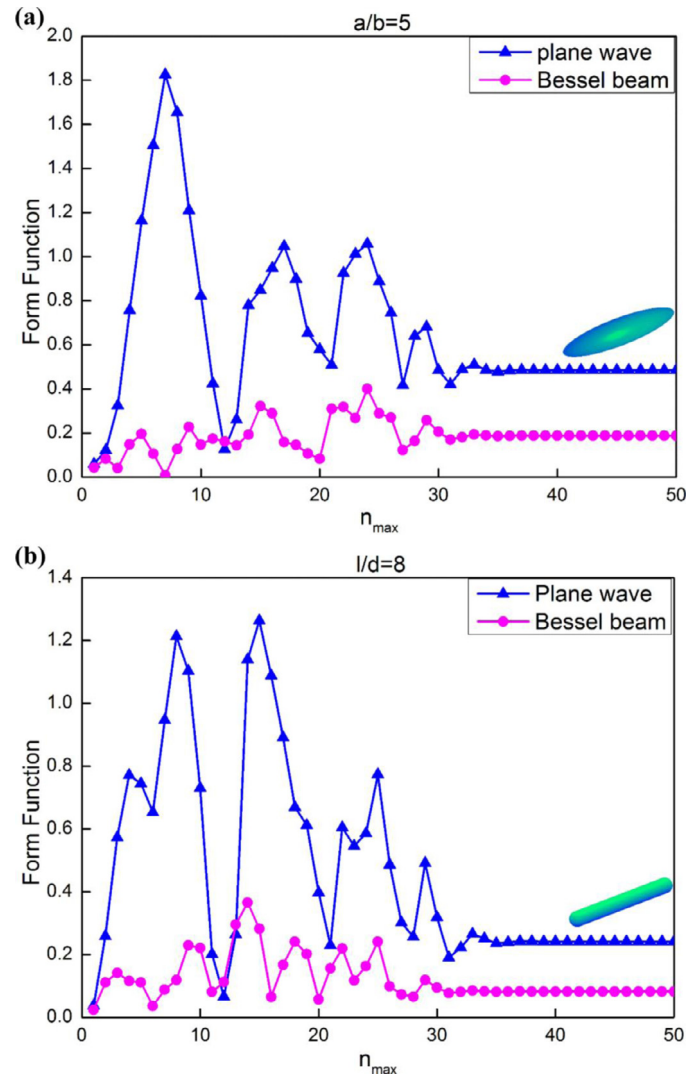


Fig. 2. Convergence study for rigid shapes with large aspect ratios. The magnitudes of the form function are shown as a function of the truncation limit n_{\max} for a rigid spheroid with aspect ratio $a/b = 5$ (panel (a)) and finite cylinder with $l/d = 8$ (panel (b)) for the dimensionless frequency $kr_0 = 30$, respectively. Both the plane wave and Bessel beam cases are given in each panel.

dependent on the dimensionless frequency, the incident angles, the half-cone angle of the Bessel beam, and the observation directions of the scattered fields. Instead, it is independent of the incident pressure amplitude, characteristic length dimension of the obstacle and the range between the target and receiver, which is in accordance with the above-mentioned normalized definition.

In the analysis of forward scattering, the target strength (TS) seems to be one of the most noteworthy parameters, for example fish detection [56]. As is known to all, TS refers to the ability of an obstacle immersed in water to scatter or reflect sound, and is essentially similar to the scattering form function. As a consequence in the following, the modified TS of the rigid spheroid and finite cylinder in Bessel beams with emphasis on the forward scattering will be mainly concerned according to the relation [56,57]

$$TS = 20 \log_{10} |f_\infty(kr_0, \theta, \varphi, \beta)| \quad (32)$$

where the TS is computed with the unit in decibels (dB) in the frequency domain and has the same parameter dependences as form function, including the dimensionless frequency, the half-cone angle of the Bessel beam, and the incident and observation directions of the fields.

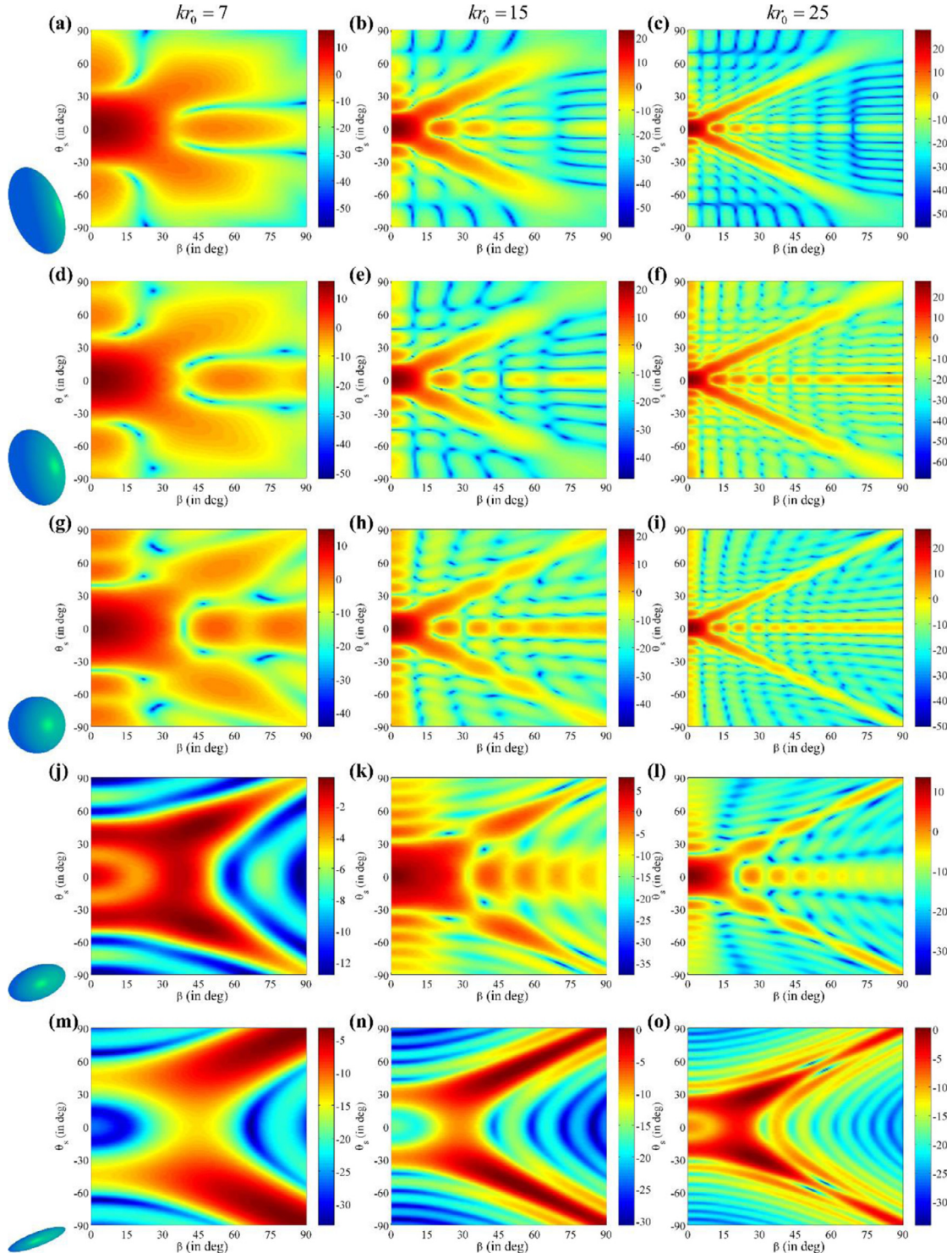


Fig. 3. The rectangular patterns of far-field target strength (TS) in the forward half-space in the (β, θ_s) domain for rigid spheroids with different aspect ratios $a/b = 1/5, 1/2, 1, 2$, and 5 , respectively. Panels (a–f) corresponds to the oblate spheroid, panels (g)–(i) to the sphere and panels (j)–(o) to the prolate spheroids. The dimensionless frequencies are given on the top of each column.

3. Numerical results and discussions

Based on the forgoing theoretical formulation, a home-made MATLAB software package was constructed accordingly and in practice verified to be exactly effective for the backscattering from rigid shapes placed in ABBs [41,42]. In this article, a parametric study has been further carried out through numerical experiments using the T -matrix method for both rigid spheroids and

finite cylinders with endcaps with variations of the aspect ratios of shapes, the half-cone angles, the dimensionless frequencies and the incident angles. It is anticipated that the present work would provide novel insights into the forward scattering in an ideal zeroth-order Bessel beam for the rigid complicated obstacles since the forward scattering performs differently with backscattering and may have important applications in engineering practices in ABBs.

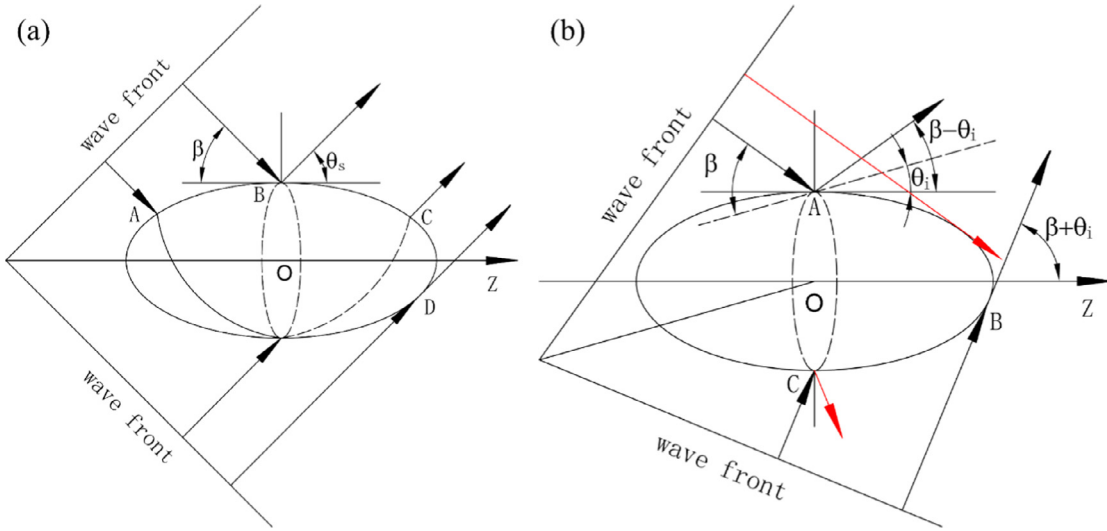


Fig. 4. Ray diagram of geometrical model for rigid spheroid with (a) end-on and (b) oblique incidence. Panel (a) describe the contribution of local direct scattering, reflection and creeping waves. Panel (b) shows the ray traces under oblique incidence with $\beta > \theta_i$.

3.1. Convergence study and accuracy discussion

Before the parametric experiments, a brief discussion on convergence and accuracy is given at first which could make all the numerical results convincing. As stated above, the infinite summation in Q matrix must be truncated at an appropriate limit n_{\max} from the standpoint of numerical computation. Therefore, convergence tests have been conducted for large-aspect-ratio rigid spheroids and finite cylinders with hemispheres in both the ordinary plane wave and the Bessel beam cases. As shown in Fig. 2 that the form functions in the forward direction of the beam axis ($\theta_s=0^\circ$) were curved versus the maximum truncation limit n_{\max} . The half-cone angle β of the considered zeroth-order Bessel beam is set as 45° . Specially, $\beta=0^\circ$ gives the limiting case of the ordinary plane wave, which is also plotted in the figure. Panel (a) of Fig. 2 depicts the forward scattering magnitude of dimensionless form functions for a rigid fixed (immovable) prolate spheroid with aspect ratio $a/b = 5$ for $kr_0=30$ at end-on incidence ($\theta_i=0^\circ$), while panel (b) corresponds to the forward scattering magnitude of dimensionless form functions for a rigid cylinder having two hemisphere endcaps with aspect ratio $l/d = 8$ for $kr_0=30$ at end-on incidence. Here, it should be noted that r_0 is actually the radius of the sphere circumscribed the spheroid or the finite cylinder, leading to $r_0=a$ for a prolate spheroid, $r_0=b$ for an oblate spheroid and $r_0=l-h+e$ for a finite cylinder with endcaps. As observed, all the curves show a good convergence to the stable and accurate solutions even in a relatively high frequency region ($kr_0=30$). In addition, the relative convergence error of the dimensionless form function (as a function of n_{\max}) could be evaluated by

$$\varepsilon(n_{\max}) = \left| \frac{f_\infty(n_{\max}) - f_\infty(N_{\max})}{f_\infty(N_{\max})} \right| \quad (33)$$

where $f_\infty(N_{\max})$ is the converged value of the form function computed at the truncation limit $N_{\max}=50$. Indeed, for all the above convergence tests, the relative convergence error could reach to $10^{-8} \sim 10^{-9}$, leading to a convergent and stable solution with a negligible truncation error by using the present matrix method for both plane waves and Bessel beams.

To further verify the accuracy of the theoretical formula based on the TTM presented in Section 2 for the Bessel beam, the stability issues of the TTM method for a rigid shape with large aspect ratio are discussed subsequently. It is helpful to review the nu-

merical validations for backscattering from rigid large-aspect-ratio obstacles in Bessel beams as shown in both Fig. 2 of [41,42] (not given here for brevity). It could be anticipated that our home-made codes based on TMM would perform exactly and efficiently by changing the parameters in observation directions for forward scattering since it was verified and validated for the backscattering cases. As is known to all, the partial-wave series solution in spherical coordinates could provide exact theoretical analysis on the scattering for spheres and infinite cylinders in ABBs, however, it may fail to compute the scattering for large-aspect-ratio aspherical geometries due to the fact that there may be ill-conditions in matrix inversion procedures through numerical implementation, leading to the system of linear equations being unsolvable. Likewise, it is also necessary to note that the TTM with standard spherical formulation is not always stable for geometry with large aspect ratio, because the elements of the Q matrix in Eq. (29) with $n > n'$ suffer from numerical cancellation noise during the surface integral procedures. Fortunately, as pointed out by Sarkissian et al. [37], the TTM based on standard formulations can still stable for rigid shapes with large aspect ratios because rotational symmetry could result in the symmetries of both the Q matrix and the transition matrix in those cases. Considering the matrix symmetry, in the numerical implementations with the home-made MATLAB package, we only compute the elements in the Q matrix with $n < n'$, which can be integrated accurately over the surface. While the elements of Q with $n > n'$, which suffer from numerical cancellation noise, are obtained by reflecting the elements with $n < n'$ across the diagonal. As a result, the full Q matrix could be obtained with numerical cancellation noise and accordingly, the transition matrix can be computed stably. Furthermore, the stability can be also guaranteed by using methods of Sarkissian et al. [37] and Doicu et al. [58] for rigid shapes with an asymmetric Q matrix. For non-rigid shapes, the TTM based on spheroidal formulation [59] or the approaches in the more recent work of Waterman [60] and Lim [40] can be applied to ensure the stability. However, those cases are outside the scope of the present investigation. Consequently, based on the convergence study and stability discussion of accuracy, it will be reasonable to believe that the present method could be regarded as an effective tool to exploit the features of forward scattering from rigid complicated obstacles with large aspect ratios placed in a zeroth-order Bessel beam.

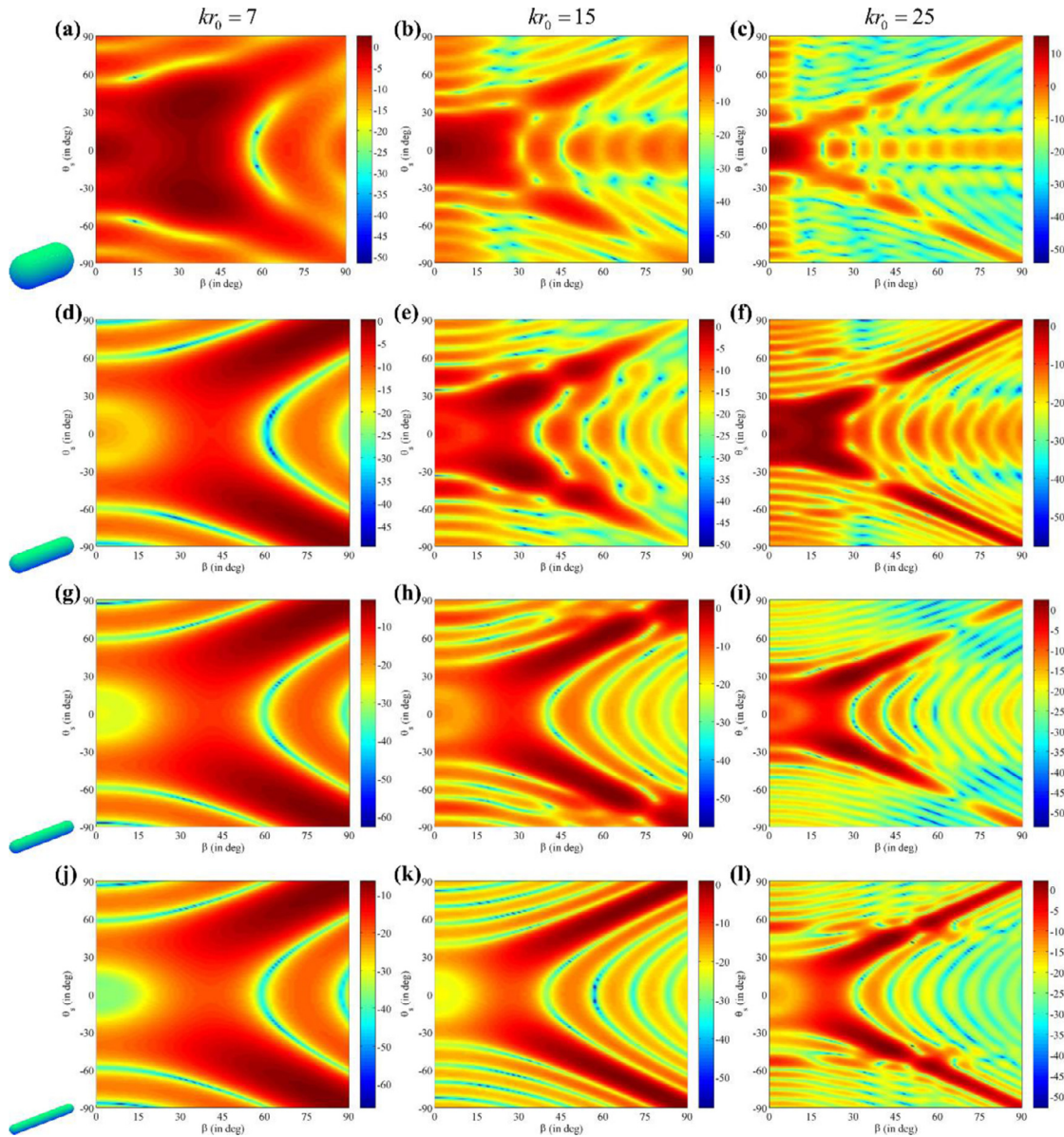


Fig. 5. Like Fig. 3 except that the rigid finite cylinders with respective aspect ratios $l/d = 2, 4, 6$ and 8 are considered.

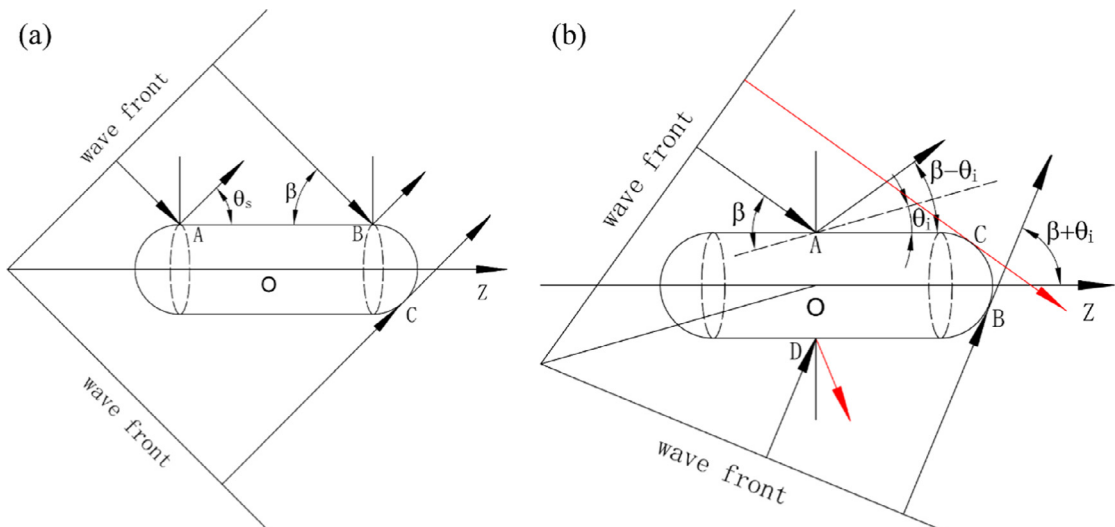


Fig. 6. Like Fig. 4 except for a rigid finite cylinder.

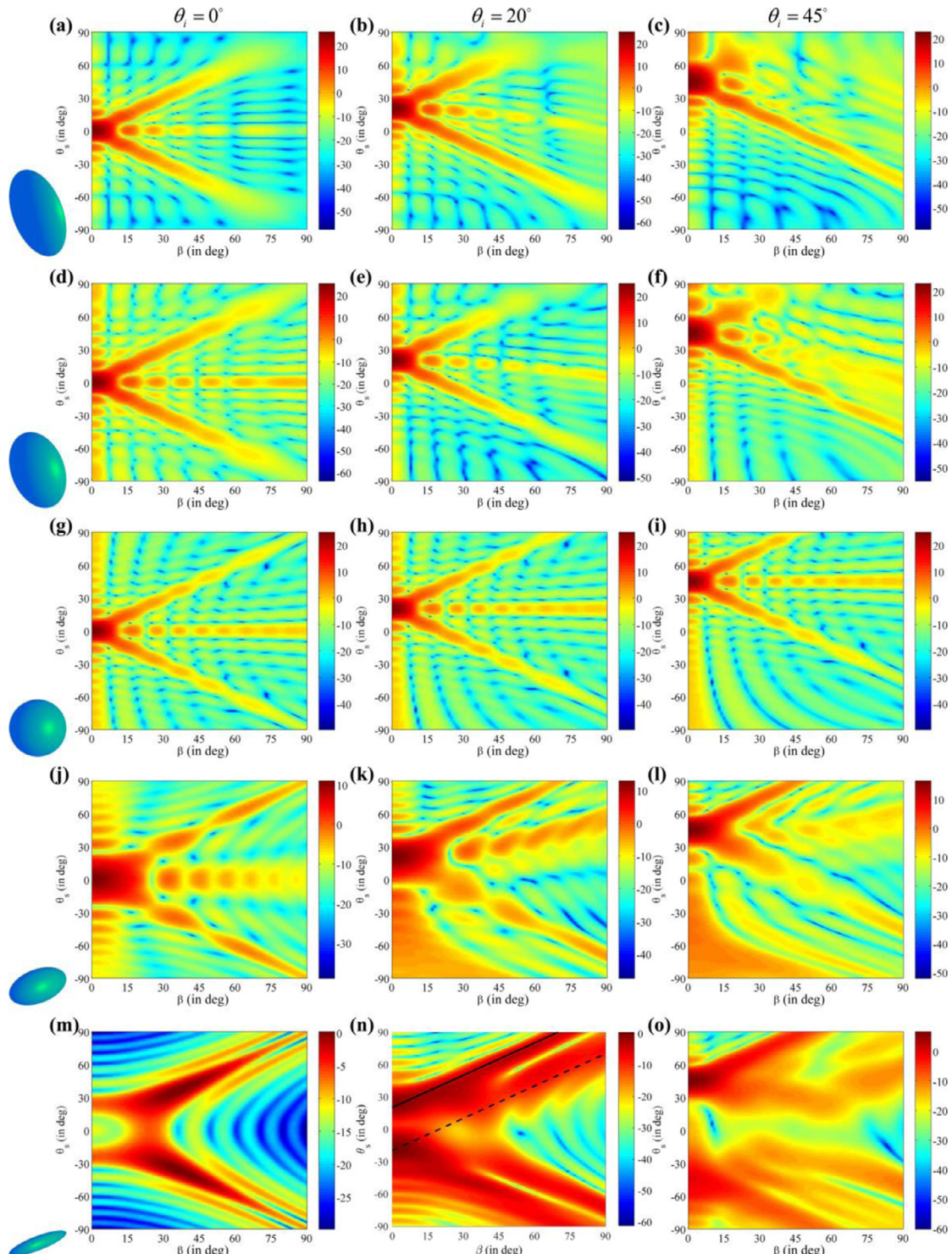


Fig. 7. The rectangular patterns of far-field target strength (TS) in the forward half-space in the (β, θ_s) domain for rigid spheroids with different aspect ratios as those in Fig. 3, with emphasis on the incident angle θ_i (given on the top of each column). The dimensionless frequency is set as $kr_0=20$ for all cases. In panel (n), the black solid line describes $\theta_s=\beta+\theta_i$, while the black dash line is $\theta_s=\beta-\theta_i$.

3.2. Scattering in forward half-space with different dimensionless frequency

Consider the case of a rigid fixed spheroid or finite cylinder placed on the axis ($\theta_i=0^\circ$) of a monochromatic zeroth-order Bessel beam with different dimensionless frequency (kr_0). The forward half-space of observation is employed with $\theta_s=[0^\circ, 90^\circ]$ and $\theta_s=[270^\circ, 360^\circ]$ (shown as $[-90^\circ, 0^\circ]$ in the following figures).

Under the on-axis incidence, the rotational symmetry of both the incident zeroth-order ABB and obstacles will lead to a rotationally symmetric scattering fields intuitively, however, this will not apply to the oblique incidence case.

Fig. 3 illustrates the far-field target strength (TS) of rigid spheroids with different aspect ratios place in the zeroth-order Bessel beams with respective dimensionless frequencies $kr_0=7, 15, 25$ (given explicitly on the top of each column). The TS is calcu-

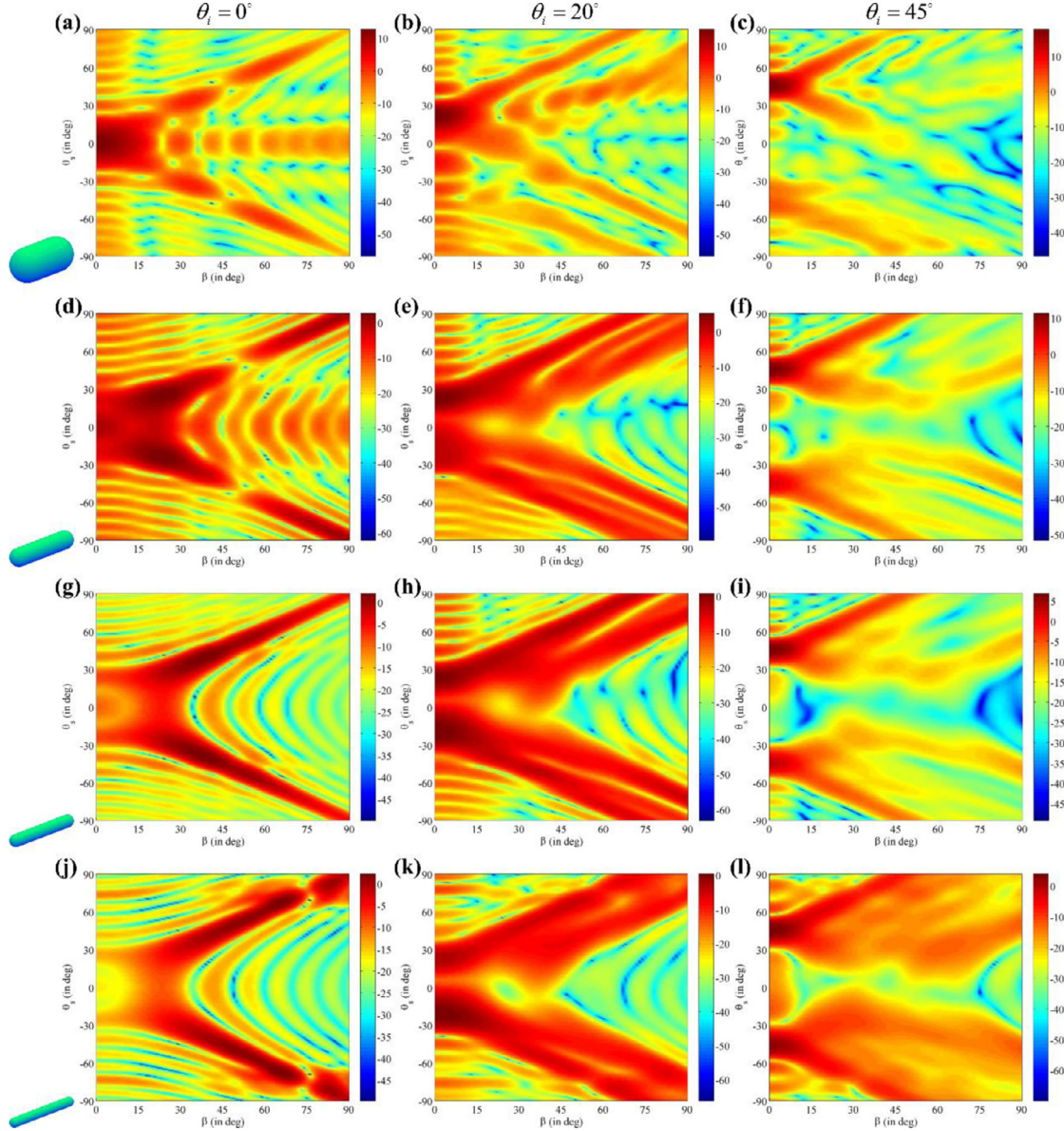


Fig. 8. Like Fig. 7 except that the rigid finite cylinders with respective aspect ratios $l/d = 2, 4, 6$ and 8 are considered.

lated as a function of both the half-cone angle β and the scattering angle θ_s which is exhibited by rectangular patterns in the (β, θ_s) domain. Panels (a)-(o) depict the rectangular plots of TS for rigid spheroids translating from oblate into prolate with aspect ratios $a/b = 1/5, 1/2, 1, 2$ and 5 , respectively. Note that the sphere case ($a/b = 1$) was computed and discussed by one of the present authors using the partial-wave series solution and the ray diagram for construction of geometric model of reflection contributions was also given there [9]. The TTM used here concentrates on the forward scattering for aspherical cases, namely, the spheroid and end-capped cylinder with finite length and some more new features have been found and explained. As shown in Fig. 3, the symmetry about the z axis ($\theta_s=0^\circ$) occurs in all the scattering patterns (in the $\varphi_s=0^\circ$ section) as we expect because of the rotational symmetry of the incident wave and the scatterers. Consider first the symmetry evident in Fig. 3 for the case of a sphere. An angle exchange symmetry $TS(\beta, \theta_s)=TS(\theta_s, \beta)$ is evident for each of the kr_0 value displayed. That symmetry was originally described by Marston, Eq. (12a) of [9], for all spheres centered on a zeroth-order Bessel beam, not just the case of rigid spheres.

The exchange symmetry in the scattering involving the half-cone β and scattering angle θ_s is also observed not only for the rigid sphere but also for the (oblate and prolate) spheroids, especially in the high frequency (the third column of Fig. 3). This phenomenon may due to the contribution of the local directed forward waves in Bessel beams. The ray diagram of a rigid spheroid under a zeroth-order ABBs at end-on incidence is described as panel (a) of Fig. 4. The influence of the reflected contributions will be discussed in detail for oblique incidences in next section. For most cases, the intense ridges of TS begin at $(\beta, \theta_s)=(0^\circ, 0^\circ)$, vary nearly linearly across the rectangular pattern, and end at $(\beta, \theta_s)=(90^\circ, \pm 90^\circ)$. It is interesting to find that the above rule fails for a prolate spheroid with large aspect ratio (Panels (m)-(o)) when the Bessel beam is close to a plane wave ($\beta=0^\circ$) and θ_s are small (i.e. the region near $(\beta, \theta_s)=(0^\circ, 0^\circ)$). This is due to the small cross-section area of the elongated spheroid in the plane normal to the direction of the incident waves and can be interpreted by the *optical cross-section theorem* that the far-field forward scattering amplitude is proportional to the geometric cross-section of the obstacle perpendicular to the incident waves [61]. In addition in the second and third

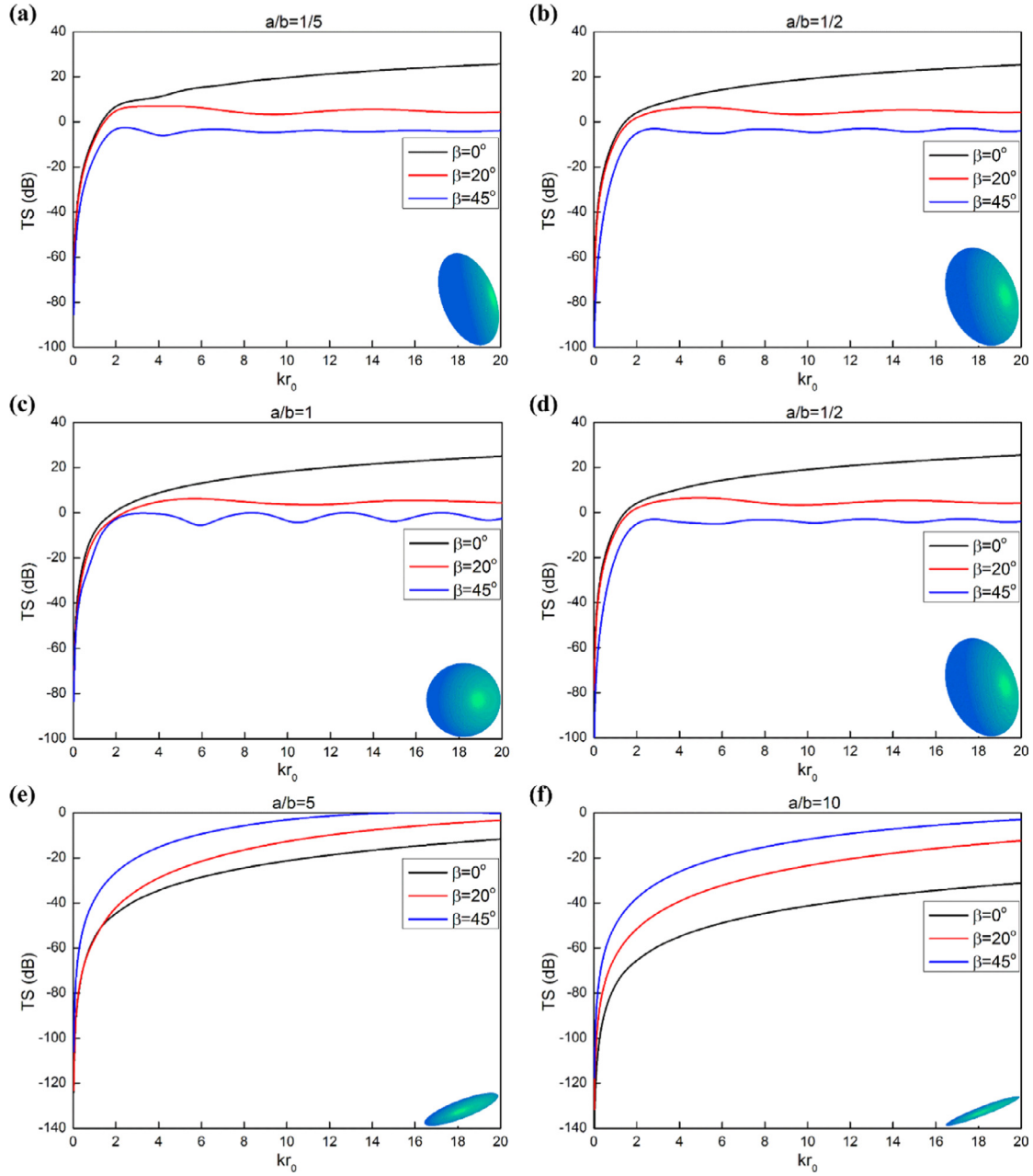


Fig. 9. The magnitudes of TS for rigid spheroids in far-field local forward scattering ($\theta_s=\beta$) varying with the dimensionless frequency kr_0 .

columns, there is a decreasing trend of the maximum magnitude of TS from the oblate to prolate spheroids which usually occurs at $(\beta, \theta_s)=(0^\circ, 0^\circ)$ (except for the extremely elongated spheroid with $a/b = 5$) because of the decrease in their cross-section areas. This phenomenon further imply the correctness of the optical theorem. Furthermore, several ridges and valleys are observed and the numbers of them increase as the dimensionless frequency kr_0 increases. The interference of the scattering and diffraction with different wave lengths would help to understand the results. Except for the contributions of the local direct forward scattering and the reflection, the creeping waves will also contribute to the scattering in the forward half-space, with one geodesic of the creeping wave described in Fig. 4(a). However, in the high frequency region (generally $kr_0 \geq 10$), the influence of creeping waves will be neglected because the damping is large with a high curvature near the end and small wavelength [62].

Panels (a)-(l) of Fig. 5 depicts the rectangular patterns of the far-field TS for the rigid finite cylinder with hemisphere endcap having aspect ratios $l/d = 2, 4, 6$ and 8 , respectively. The parameters of the incident waves are the same as those for spheroids above. Similarly, the symmetry about the z axis is observed again for all patterns and for most cases in the region with a relatively large half-cone, the exchange symmetry in the scattering involving β and θ_s is obvious to observe. It is interesting to note that the rectangular patterns for cylinder with $l/d = 2$ are similar with those of spheroid with aspect ratio $a/b = 2$; while the rectangular patterns for large aspect ratio (e.g. $l/d = 6$ and 8) have much similarities with those of pattern of large-aspect-ratio spheroid, respectively. Panels (d), (g) and (j) correspond to the far-field scattering pattern of cylinder with $l/d = 4, 6$ and 8 for dimensionless frequency $kr_0=7$, respectively. The rectangular patterns show great similarities with different aspect ratios, and more interestingly, two symmetric curves about the z axis with low TS occurs

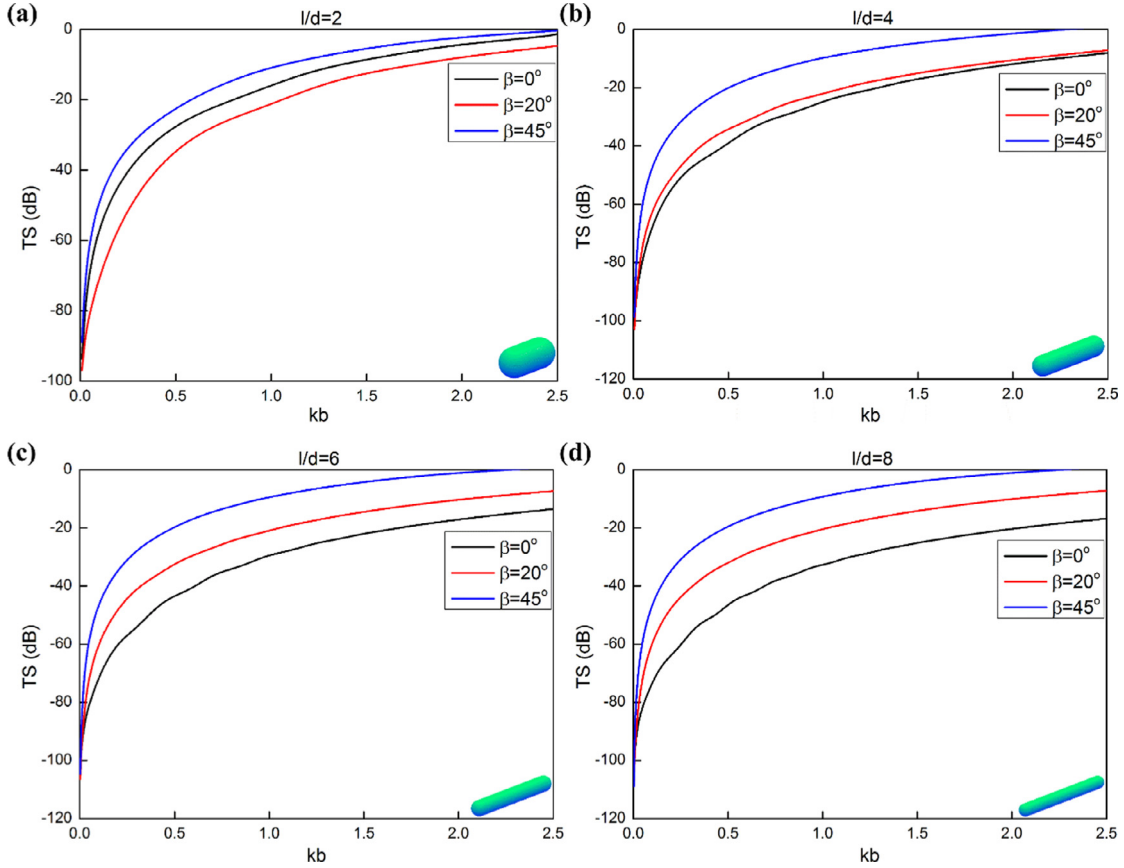


Fig. 10. The magnitudes of TS for rigid finite cylinders in far-field local forward scattering ($\theta_s=\beta$) varying with the dimensionless frequency kb .

in each panel, which begin at $(\beta, \theta_s) \approx (0^\circ, 60^\circ)$ and end at $(\beta, \theta_s) \approx (60^\circ, \pm 90^\circ)$ (taking the region above $\theta_s=0^\circ$ for example). Meanwhile, the TS also shows a weak trend in the broadside observations ($\theta_s=\pm 90^\circ$) when the half-cone angle is small. The geometrical ray diagram for the finite cylinder under ABBs illumination with end-on incidence is depicted in Fig. 6(a) and the models are helpful to explain some features of the numerical results.

3.3. Scattering in forward half-space with arbitrary angles of incidence

The far-field TS of both the rigid spheroids and finite cylinders in the forward half-space are further investigated with different incident angles, such that $\theta_i=0^\circ$ (end-on incidence), 20° and 45° (oblique incidence). Here, the half-space is defined as the same as before with the scattering angle $\theta_s=[0^\circ, 90^\circ]$ and $\theta_s=[270^\circ, 360^\circ]$, and the end-on incidence cases is here not the kernel since it has been discussed before. Fig. 7 gives the rectangular patterns for rigid spheroid with different aspect ratios as same as those in Fig. 3, having a dimensionless frequency $kr_0=20$. For the oblique incidences as shown in the second and third columns, the symmetry about the z axis is no more occurs in the scattering pattern. For the rigid sphere shown in panels (g)–(i), the scattering pattern seems still to have a symmetry but at present the symmetry is $\theta_s=\theta_i$ instead of the z axis. Indeed, the whole scattering fields will still keep symmetric since the incident axis is always the symmetric axis of the sphere. While for the spheroids, the symmetry of the scattering patterns disappear in the given oblique angles of incidence (shown in the second and third columns except for the sphere) unless the incident axis coincides with the symmetric axes of the spheroids. Moreover, the scattering patterns of the oblate spheroids are quite different from those of the prolate. For

the oblate cases, the intense ridges of TS begin at $(\beta, \theta_s)=(0^\circ, \theta_i)$, vary nearly linearly across downward the rectangular pattern, and end at $(\beta, \theta_s)=(0^\circ, \theta_i-90^\circ)$ in the region below $\theta_s=\theta_i$. The linear trend seems not obvious in the region above $\theta_s=\theta_i$, especially for the large oblique angle of incidence case ($\theta_i=45^\circ$). Note that for the oblate spheroid, the reflection wave has a large contribution to the scattering in backward half-space instead of the forward half-space. While for the prolate spheroid cases, it could be found for large-aspect-ratio spheroid (panels (n) and (o)) there are two obvious beginnings of the intense ridges of TS, i.e. $(\beta, \theta_s)=(0^\circ, \theta_i)$ and $(\beta, \theta_s)=(0^\circ, -\theta_i)$, owing to the fact that both the local forward scattering ($\theta_s=\beta+\theta_i$, black solid line in panel (n)) and the reflected contributions ($\theta_s=\beta-\theta_i$, black dash line in panel (n)) to the scattering in the forward half-space dominate the scattering patterns. The ray diagram of the spheroid in Fig. 4(b) with the corresponding relationship among the angles and the *optical cross-section theorem* are helpful to interpret these phenomena.

Next, the forward scattering patterns of finite cylinder with hemisphere endcaps illuminated by the obliquely incident Bessel beam are shown in Fig. 8. The aspect ratio are chosen as the same as those in Fig. 5 and the incident angles are 0° , 20° and 45° , respectively. Note that the intense ridges of TS begins at both $(\beta, \theta_s)=(0^\circ, \theta_i)$ and $(\beta, \theta_s)=(0^\circ, -\theta_i)$, and each has a large region in the rectangular patterns for oblique incidence cases. The scattering patterns for rigid cylinder with aspect ratio $l/d \geq 4$ at present are similar to those of the large-aspect-ratio spheroid $a/b=5$ under the same incident beams correspondingly. The geometric ray diagram depicted in Fig. 6 help to understand the conclusion. Here we take the cylinder with $l/d=6$ with incident angle $\theta_i=20^\circ$ (panel (h)) as an example in the rectangular region above $\theta_s=0^\circ$. In the geometrical model with different ray traces,

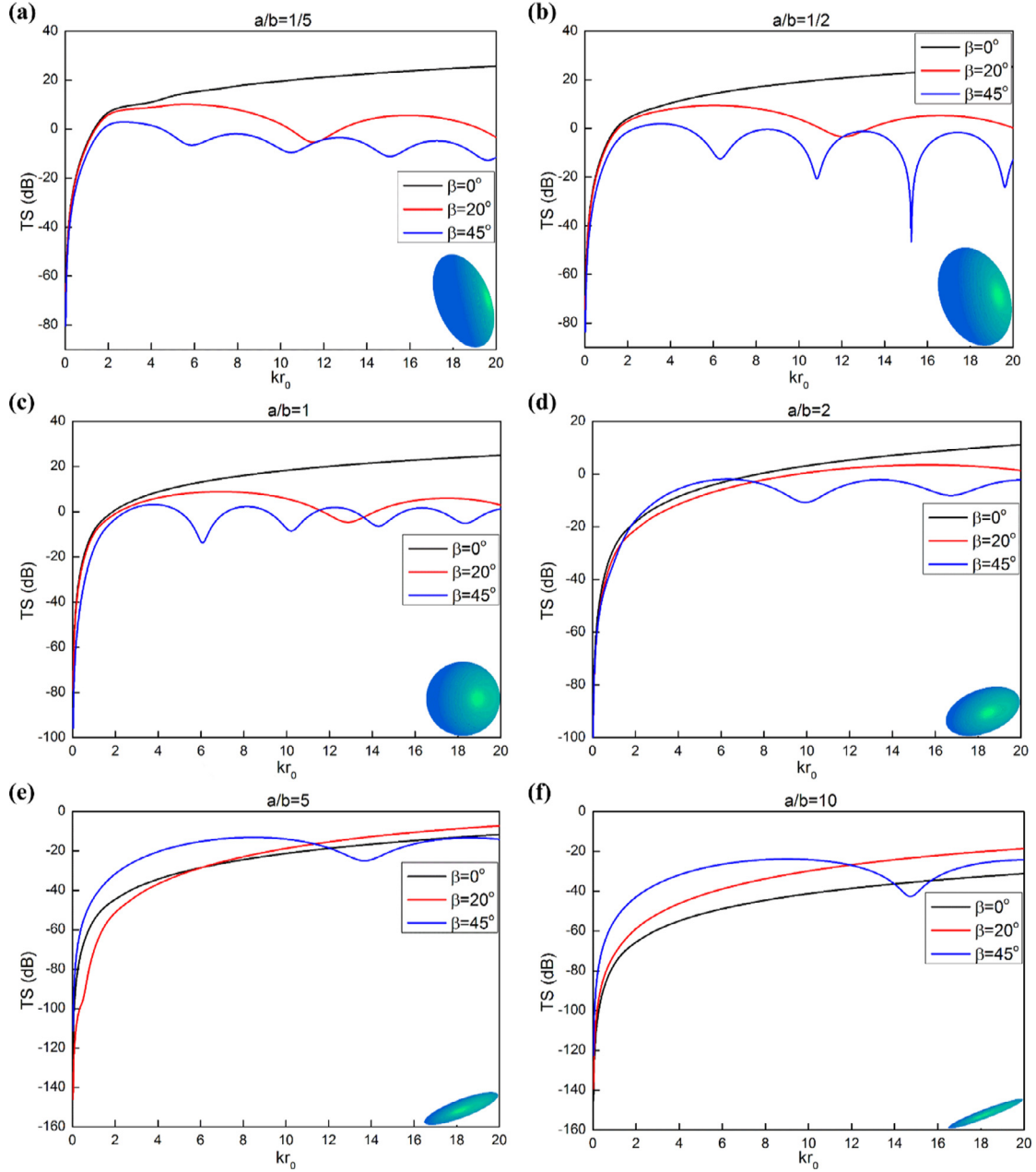


Fig. 11. Like Fig. 9 except that $\theta_s=0^\circ$.

the local direct forward scattering happens at a scattering angle $\theta_s=\beta+\theta_i=\beta+20^\circ$, while the reflected waves contribute at the scattering angle $\theta_s=\beta-\theta_i=\beta-20^\circ$ (consider $\beta>\theta_i$). The ray diagram could successfully interpret the two bands of intense TS above $\theta_s=0^\circ$. Specifically, the upper band is attributed to the local direct forward scattering and the central line of the band ends at $(\beta, \theta_s)=(70^\circ, 90^\circ)$, while the lower band corresponds to the reflection and its central line of the band ends at $(\beta, \theta_s)=(90^\circ, 70^\circ)$. Similarly, the bands of intense TS in the rectangular region under $\theta_s=0^\circ$ could also use ray diagram to describe, which is shown with the red ray traces. This mechanism could also apply to the spheroid case with large aspect ratio (see panel (n) in Fig. 7).

3.4. Local forward scattering (scattering angle equals half-cone angle)

In practice, the forward scattering plays a significant role in the direction of the incident axis for the plane wave. However, due to

the novel properties for the Bessel beams (which may be considered as the superposition of plane waves), the forward scattering is influenced by both the incident angles and the characteristic parameter (half-cone angle) of Bessel beams. Here we classified the forward scattering into two categories: the local forward scattering ($\theta_s=\beta$) and the total forward scattering ($\theta_s=\theta_i$). Only the end-on incidence will be considered. Note that the local forward scattering amplitude having $\theta_s=\beta$ has been shown to be closely related to the extinction cross section for objects illuminated by Bessel beams [18,63].

The magnitudes of TS for rigid spheroids in far-field local forward scattering varying with the dimensionless frequency kr_0 are given in Fig. 9, with aspect ratios $a/b = 1/5, 1/2, 1, 2, 5$ and 10 , respectively. The incident Bessel beams are chosen with the half-cone angles $\beta=0^\circ$ (plane wave), 20° and 45° , given in each panel explicitly. Intuitively, the magnitudes of forward scattering lack the oscillatory features that exist in the backscattering (see

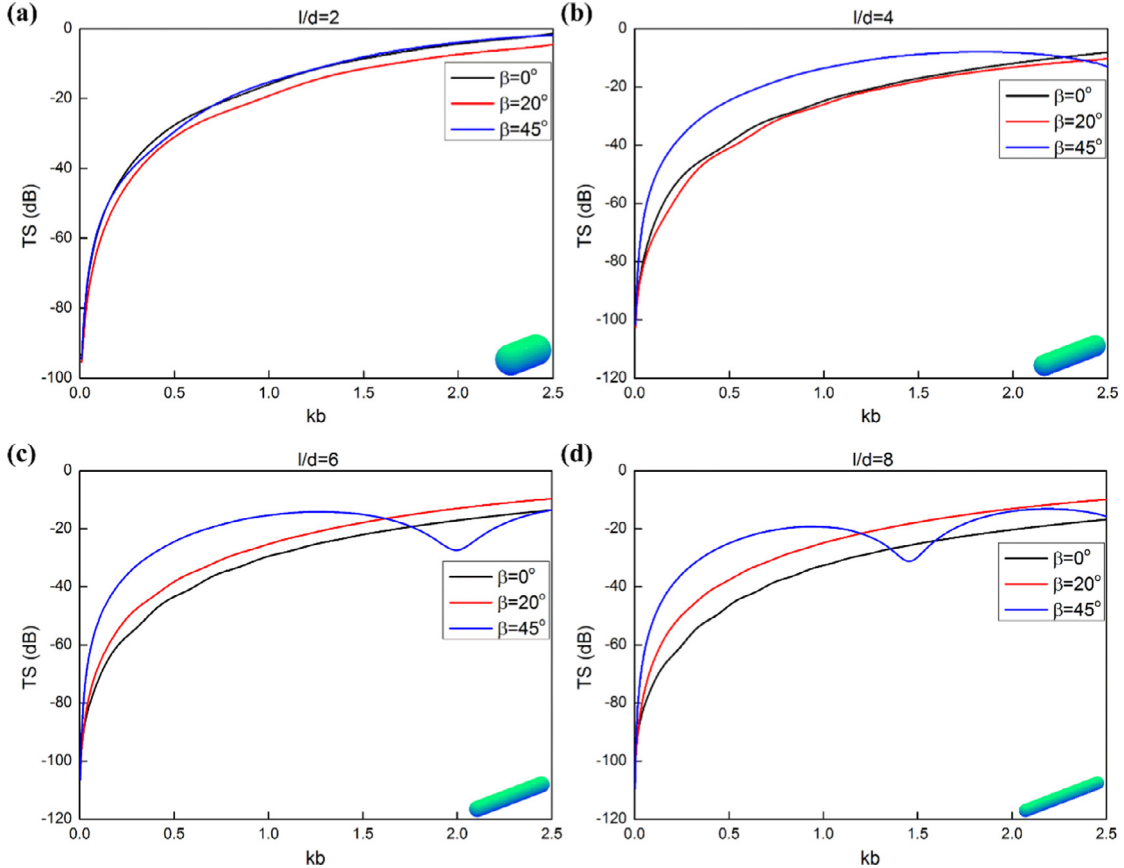


Fig. 12. Like Fig. 10 except that $\theta_s=0^\circ$.

Fig. 3 in [41]). This phenomenon may be interpreted as the dominant mechanism of the direct arrival waves to the local forward scattering. As stated by the optical theorem (which is according to the Huygens-Fresnel principle and the Babinet's principle), the forward scattered field is proportional to the geometrical cross-section of the obstacle and meanwhile inversely proportional to the incident wavelength (i.e., proportional to dimensionless frequency kr_0). Taking the spheroids in plane waves as examples (black solid lines in Fig. 9), the magnitudes of TS in the high frequency region decrease continuously from the extremely oblate to elongated spheroids (panels (a)-(f)), owing to the fact that the cross sections of these spheroids in the plane normal to the incident waves continue to reduce under these circumstances. Moreover, because of the geometry differences between the oblate and prolate spheroids, the cross sections will change differently. As the half-cone angle increases, the incidence wave deviates further from the incident axis, leading to a decrease of the cross sections for the oblate spheroid while an increase for the prolate spheroids. This coincides well with the results shown in most panels with larger aspect ratios for both the oblate and prolate spheroids. As claimed that the forward scattering is always likely to be stronger than backscattering [1,3], which is also implied here. For the rigid sphere case, the form function modulus of backward scattering in plane waves tends to be 1 in the high frequency region, such that the TS = 0. The panel (c) shows that the TS magnitude of the rigid sphere in plane waves is equal to about 20, which is actually much stronger than the backscattering TS.

Fig. 10 describes magnitude of TS for rigid cylinder with hemisphere endcap in the far-field local forward scattering with respective aspect ratios $l/d = 2, 4, 6$ and 8. In order to compare with the

backscattering results in [42], the abscissa is set as kb instead of kr_0 . As noticed from these panels, the results of local forward are less sensitive to dimensionless frequency than those of backscattering, leading to no oscillations. Similarly as the prolate spheroid cases, the magnitudes of TS in the local forward scattering increase when β increases for the rigid finite cylinder with large aspect ratios (except panel (a)).

3.5. Total forward scattering (scattering angle equals incident axial angle)

Furthermore, the total forward scattering ($\theta_s=\theta_i$) results for spheroids and cylinders are also plotted in Figs. 11 and 12, respectively. The aspect ratios of spheroids and cylinders are the same as those in Figs. 9 and 10, respectively. It is obvious to observe that for the Bessel beam incidence, more oscillations occurs for the magnitudes of TS versus the dimensionless frequency and the oscillated peaks seem to increase with the increase of half-cone angles. In addition, the changing trends of total forward scattering magnitudes in the Bessel beams with respect to those in plane waves are uncertain under the present circumstances. This is due to the fact that with a half-cone angle of the Bessel beam vectors, the direct forward scattering wave is at the direction have an angular β with respect to the incident axis, rather than the total forward scattering direction (the direction of the beam axis). In consequence, the optical theorem fails to interpret the results in Figs. 11 and 12. The total forward scattering is actually attributed to the combined contributions of a series of different creeping waves from the edges of shadow [62] and a reflected waves (ray diagram for sphere case given in [9]).

4. Concluding remarks

The *T*-matrix method is successfully applied to investigate the acoustic scattering from rigid spheroids and finite cylinders with hemisphere endcaps illuminated by an idealized zeroth-order Bessel beam with arbitrary incidence, with the emphasis on the scattering in the forward half-space. The present work provide several new insights into the novel characteristics of the forward scattering from rigid typical aspherical shapes even with a large aspect ratio, which helps to understand several characteristics of the acoustic Bessel beam scattering with various obstacles. The present TTM and the previous PWSM complement each other with their own advantages and disadvantages, such that a wider range of problems in the context of ABBs could be explored. The geometrical models with ray diagram are proposed and *optical cross-section theorem* is applied, leading to a good interpretation of the forward scattering mechanisms for ABBs. Note that the TMM has been demonstrated effective to calculate the optical radiation forces and torques [64–66], which will inspire the authors to extend the TTM for investigations on acoustic radiation forces and torques both in ordinary and helicoidal ABBs [67] since the radiation pressures are much larger in acoustics than those in optics with the same field intensity [68].

Acknowledgments

This work is supported by the National Natural Science Foundation of China under Grant No. 51579112. P.L. Marston acknowledges support from ONR. Z.G. thanks HUST for support, and Timothy Daniel in WSU for useful suggestions to improve the presentation of this manuscript.

References

- [1] Gillespie B, et al. Littoral target forward scattering. In: Proceedings of the 23rd international symposium on acoustical imaging. Plenum Press; 1997.
- [2] Sabra KG. Experimental demonstration of a high-frequency forward scattering acoustic barrier in a dynamic coastal environment. *J Acoust Soc Am* 2010;127:3430–9.
- [3] Lei B, Yang K, Ma Y. Physical model of acoustic forward scattering by cylindrical shell and its experimental validation. *Chin Phys B* 2010;19:054301.
- [4] Zverev VA, et al. Experimental studies of sound diffraction by moving inhomogeneities under shallow-water conditions. *Acoust Phys* 2001;47:184–93.
- [5] Matveev AL, Spindel RC, Rouseff D. Forward scattering observation with partially coherent spatial processing of vertical array signals in shallow water. *IEEE J Oceanic Eng* 2007;32:626–39.
- [6] Lei B, Ma Y, Yang K. Experiment Observation on acoustic forward scattering for underwater moving object detection. *Chin Phys Lett* 2011;28:034302.
- [7] Lei B, Yang K, Ma Y. Range estimation for forward scattering of an underwater object with experimental verification. *J Acoust Soc Am* 2012;132:EL284–9.
- [8] Lei B, Yang K, Ma Y. Forward scattering detection of a submerged object by a vertical hydrophone array. *J Acoust Soc Am* 2014;136:2998–3007.
- [9] Marston PL. Scattering of a Bessel beam by a sphere. *J Acoust Soc Am* 2007;121:753–8.
- [10] Marston PL. Angle exchange symmetries for acoustic Bessel beam scattering and the radiation force on spheres. *J Acoust Soc Am* 2013;134:4010.
- [11] Chen J, et al. Optical pulling force. *Nat Photonics* 2011;5:531–4.
- [12] Li R, et al. Analysis of radiation pressure force exerted on a biological cell induced by high-order Bessel beams using Debye series. *J Quant Spectrosc Radiat Transf* 2013;126:69–77.
- [13] Marston PL. Surprises and anomalies in acoustical and optical scattering and radiation forces. *J Quant Spectrosc Radiat Transf* 2015;162:8–17.
- [14] Wang JJ, et al. General description of circularly symmetric Bessel beams of arbitrary order. *J Quant Spectrosc Radiat Transf* 2016;184:218–32.
- [15] Li R, et al. Optical torque on a magneto-dielectric Rayleigh absorptive sphere by a vector Bessel (vortex) beam. *J Quant Spectrosc Radiat Transf* 2017;191:96–115.
- [16] Marston PL. Axial radiation force of a Bessel beam on a sphere and direction reversal of the force. *J Acoust Soc Am* 2006;120:3518–24.
- [17] Marston PL. Scattering of a Bessel beam by a sphere: II. Helicoidal case and spherical shell example. *J Acoust Soc Am* 2008;124:2905–10.
- [18] Zhang L, Marston PL. Axial radiation force exerted by general non-diffracting beams. *J Acoust Soc Am* 2012;131:EL329–35.
- [19] Zhang L, Marston PL. Optical theorem for acoustic non-diffracting beams and application to radiation force and torque. *Biomed Opt Express* 2013;4:1610–17.
- [20] Baresch D, Thomas JL, Marchiano R. Three-dimensional acoustic radiation force on an arbitrary located elastic sphere. *J Acoust Soc Am* 2012;133:25–36.
- [21] Baresch D, Marchiano R, Thomas JL. Three-dimensional analysis of the acoustic radiation pressure: application to single-beam acoustical tweezers. In: Proceedings of meetings on acoustics ICA2013. ASA; 2013.
- [22] Riaud A, et al. Taming the degeneration of Bessel beams at an anisotropic-isotropic interface: toward three-dimensional control of confined vortical waves. *Phys Rev E* 2015;92:063201.
- [23] Durnin J, Miceli J, Eberly JH. Diffraction-free beams. *Phys Rev Lett* 1987;58:1499–501.
- [24] Piestun R, Shamir J. Generalized propagation-invariant wave fields. *J Opt Soc Am A* 1998;15:3039–44.
- [25] Bouchal Z. Nondiffracting optical beams: physical properties, experiments, and applications. *Czech J Phys* 2003;53:537–78.
- [26] López-Mariscal C, Gutiérrez-Vega JC. The generation of nondiffracting beams using inexpensive computer-generated holograms. *Am J Phys* 2007;75:36–42.
- [27] Bouchal Z, Wagner J, Chlup M. Self-reconstruction of a distorted nondiffracting beam. *Opt Commun* 1998;151:207–11.
- [28] Garces-Chavez V, et al. Simultaneous micromanipulation in multiple planes using a self-reconstructing light beam. *Nature* 2002;419:145–7.
- [29] Fahrbach FO, Simon P, Rohrbach A. Microscopy with self-reconstructing beams. *Nat Photonics* 2010;4:780–5.
- [30] Belafhal A, Ez-Zaray L, Hricha Z. A study of nondiffracting Lommel beams propagating in a medium containing spherical scatterers. *J Quant Spectrosc Radiat Transf* 2016;184:1–7.
- [31] Marston PL. Self-reconstruction property of fractional Bessel beams: comment. *J Opt Soc Am A* 2009;26:2181.
- [32] Zhang L, Marston PL. Geometrical interpretation of negative radiation forces of acoustical Bessel beams on spheres. *Phys Rev E* 2011;84:035601.
- [33] Zhang L, Marston PL. Acoustic radiation torque and the conservation of angular momentum. *J Acoust Soc Am* 2011;129:1679–80.
- [34] Mitri FG. Axisymmetric Scattering of an acoustical Bessel beam by a rigid fixed spheroid. *IEEE Trans Ultrason Ferroelectr Freq Control* 2015;62:1809–18.
- [35] Mitri FG. Acoustic scattering of a Bessel vortex beam by a rigid fixed spheroid. *Ann Phys* 2015;363:262–74.
- [36] Waterman PC. New formulation of acoustic scattering. *J Acoust Soc Am* 1969;45:1417–29.
- [37] Sarkissian A, Gaumond CF, Dragonette LR. T-matrix implementation of forward scattering from rigid structures. *J Acoust Soc Am* 1993;94:3448–53.
- [38] Waterman PC. T-matrix methods in acoustic scattering. *J Acoust Soc Am* 2009;125:42–51.
- [39] Ganesh M, Hawkins SC. A stochastic pseudospectral and T-matrix algorithm for acoustic scattering by a class of multiple particle configurations. *J Quant Spectrosc Radiat Transf* 2013;123:41–52.
- [40] Lim R. A more stable transition matrix for acoustic target scattering by elongated objects. *J Acoust Soc Am* 2015;138:2266–78.
- [41] Gong Z, et al. Arbitrary scattering of an acoustical Bessel beam by a rigid spheroid with large aspect-ratio. *J Sound Vib* 2016;383:233–47.
- [42] Gong Z, et al. T-matrix method for acoustical Bessel beam scattering from a rigid finite cylinder with spherical endcaps. *Ocean Eng* 2017;129:507–19.
- [43] Waterman PC. Matrix formulation of electromagnetic scattering. In: Proceedings of the IEEE. IEEE; 1965.
- [44] Mishchenko MI, Travis LD, Mackowski DW. T-matrix computations of light scattering by nonspherical particles: a review. *J Quant Spectrosc Radiat Transf* 1996;55:535–75.
- [45] Mishchenko MI, Travis LD, Lacis AA. Scattering, absorption, and emission of light by small particles. Cambridge: Cambridge University Press; 2002. p. 115–27, Secs. 5.1–5.2, 5.1.1–5.1.165–189.
- [46] Varatharajulu V, Pao Y. Scattering matrix for elastic waves. I. Theory. *J Acoust Soc Am* 1976;60:556–66.
- [47] Pao Y. Betti's identity and transition matrix for elastic waves. *J Acoust Soc Am* 1978;64:302–10.
- [48] Liu S, et al. Underwater acoustic scattering of Bessel beam by spherical shell using T-matrix method. In: Proceedings of ocean acoustics (COA) 2016 IEEE/OES China. IEEE; 2016.
- [49] Gong Z, Li W, Chai Y. Acoustic resonance scattering of Bessel beam by elastic spheroids in water. In: Proceedings of 6th international conference on computational methods (ICCM2015); 2015.
- [50] Durnin J. Exact solutions for nondiffracting beams. I. The scalar theory. *J Opt Soc Am A* 1987;4:651–4.
- [51] Stratton JA. Electromagnetic theory. New York: John Wiley & Sons; 1999. p. 107–11. Secs. 3.5–3.6.
- [52] Bostrom A. Time-dependent scattering by a bounded obstacle in three dimensions. *J Math Phys* 1982;23:1444–50.
- [53] Varadan VV, Lakhtakia A, Varadan VK. Field representations and introduction to scattering. North-Holland: Elsevier Science Publishing Company; 1991.
- [54] Crocker MJ. Handbook of acoustics. New York: John Wiley & Sons; 1998. p. 373–86. Chap. 33.
- [55] Neubauer WG, Vogt RH, Dragonette LR. Acoustic reflection from elastic spheres. I. Steady-state signals. *J Acoust Soc Am* 1974;55:1123–9.
- [56] Ye Z, Furusawa M. Modeling of target strength of swimbladder fish at high frequencies. *J Acoust Soc Jpn* 1995;16:371–9.
- [57] Furusawa M. Prolate spheroidal models for predicting general trends of fish target strength. *J Acoust Soc Jpn* 1988;9:13–24.
- [58] Doicu A, Eremin Y, Wriedt T. Acoustic and electromagnetic scattering analysis using discrete sources. New York: Academic Press; 2000.

- [59] Hackman RH, Todoroff DG. An application of the spheroidal coordinate-based transition matrix: the acoustic scattering from high aspect ratio solids. *J Acoust Soc Am* 1985;78:1058–71.
- [60] Waterman PC. T-matrix methods in acoustic scattering. *J Acoust Soc Am* 2009;125:42–51.
- [61] Born M, Wolf E. Principles of optics. England: Cambridge University Press; 1999. p. 716–24. Sec. 13.3.
- [62] Franz W, Klarke K. Diffraction by surfaces of variable curvature. *IRE Trans Antennas Propag* 1959;7:68–70.
- [63] Marston PL. Quasi-scaling of the extinction efficiency of spheres in high frequency Bessel beams. *J Acoust Soc Am* 2014;135:1668–71.
- [64] Mishchenko MI. Radiation pressure on randomly-oriented aspherical particles. *Astrophys Space Sci* 1991;180:163–9.
- [65] Nieminen TA, Rubinsztein-Dunlop H, Heckenberg NR. Calculation and optical measurement of laser trapping forces on non-spherical particles. *J Quant Spectrosc Radiat Transf* 2001;70:627–37.
- [66] Nieminen TA. Optical tweezers computational toolbox. *J Opt A* 2007;9:S196–203.
- [67] Gong Z, et al. Multipole expansion of acoustical Bessel beams with arbitrary order and location. *J Acoust Soc Am* 2017;141:EL1–5.
- [68] Thomas JL, Marchiano R, Baresch D. Acoustical and optical radiation pressure and the development of single beam acoustical tweezers. *J Quant Spectrosc Radiat Transf* 2017;195:55–65. <http://dx.doi.org/10.1016/j.jqsrt.2017.01.012>.